TÉCNICO LISBOA

Development of a Soiling Detection for Photovoltaic Modules Based On Static Cameras

Maria Macedo Paz Ferreira

Thesis to obtain the Master of Science Degree in

Energy Engineering and Management

Supervisors: Dr. Rui Pedro da Costa Neto
Dr. Peter Winkel

Examination Committee

Chairperson: Prof. Jorge de Saldanha Gonçalves Matos
Supervisor: Dr. Rui Pedro da Costa Neto
Member of the Committee: Dr. Ana Filipa da Silva Ferreira

October 2022

I declare that this document is an original work of my own authorship and that it fulfills all the requirements of the Code of Conduct and Good Practices of the Universidade de Lisboa.

Acknowledgments

First of all, I would like to thank Dr. Rui Pedro da Costa Neto and Peter Winkel for their constant guidance and extreme availability throughout the development of this Master's thesis.

These past six months have been a lifetime experience. I would like to acknowledge CIEMAT and DLR for giving me this opportunity to work on such a meaningful project and all of my colleagues in Almeria, *Dankeschön*.

I would like to express my gratitude to my family on this journey, who support me unconditionally and celebrates all my personal conquest like their own. Mother and Father for your precious teachings and for giving me the freedom to shape my future. My brothers, António and Virgílio, for the incredible connection that we have developed together. Thank you.

Thanks to my friends from São Miguel, Azores, for showing me that nothing has changed and our bonds are stronger than any geographical distance. To my basketball teammates that made the last five difficult academic years much lighter. All my friends that I met during my time at University, and helped me to enjoy "the best years of our life" while struggling with exams and studies. One last time to all of you, *Viva ao Mordomo!*

Lastly, I dedicate my Master's Thesis to my grandmother Mariana. Without her unconditional support and long calls almost every day, nothing of this would be possible. She was a true believer that if we had a candle lighting on during the exam, plus a little prayer, everything was possible. Consider this final academic project as my candle to you.

Abstract

During the operation of photovoltaic (PV) power plants, soiling reduces the generated power by 3 to 4% on the global average. For quantitative soiling analysis, measurement equipment commercially available covers only small measurement areas. Other published optical measurement methods of soiling use drones. One limitation of these methods is the short duration (around 20 minutes) of the drone flight. Continuous measurements can be enabled by static cameras, such as, surveillance camera. This study presents a method to determine the soiling of PV plants over a large area with a high resolution. Depending on the PV park, already existing cameras can be used, avoiding extra costs.

A commercially available surveillance camera captures RGB (Red, green and blue) images of the modules to be measured. The method is based on the evaluation of the light scattered by the dirt particles increasing the brightness of the module's dirty areas. In the first step of the analysis, perspective-rectified orthoimages are calculated. Then the brightness analysis is performed, considering the given geometry. The results showed for optimal conditions, that is, a clear sky, the method has a relative deviation to the electrical reference measurement of 2% to 4% and a relative error of 12% to 14% for a clear sky with some clouds. In case of adverse meteorological conditions, the accuracy decreases. In addition, iit was found that, apart from the predicted limitations of the method, one more aspect needs to be considered, which is the existence of bird drops.

Keywords: Photovoltaic solar energy, Soiling Measurements, Performance analysis.

Resumo

Durante o funcionamento das centrais fotovoltaicas, o pó/sujidade reduz a energia gerada em 3 a 4% na média global. Para a análise quantitativa da sujidade, o equipamento de medição comercialmente disponível cobre apenas pequenas áreas. Outros métodos de medição óptica de sujidade publicados utilizam drones. Uma das limitações destes métodos é a curta duração do voo do drone. Uma medição contínua é possível através de uma câmara estática, como por exemplo, uma câmara de vigilância. Este estudo apresenta um método para determinar o pó/sujidade de plantas fotovoltaicas sobre uma grande área com uma alta resolução. Dependendo do parque fotovoltaico, as câmaras já existentes podem ser utilizadas, evitando custos adicionais.

Uma câmara comercial de vigilância capta imagens RGB dos módulos a serem medidos. O método baseia-se na avaliação da luz que é dispersa pelas partículas de sujidade, que aumenta a luminosidade das zonas sujas do módulo. Na primeira etapa da análise, são calculadas ortoimagens retificadas em perspectiva. Em seguida, realiza-se a análise do brilho, considerando a respectiva geometria. Os resultados mostram que para condições ótimas, isto é, céu limpo, o método tem um desvio relativo para a sua referência elétrica de 2 a 4% e um erro relativo de 12 a 14% para um céu limpo com algumas nuvens. Em caso de condições meteorológicas adversas, a precisão é reduzida. Foi também concluído que, para além das limitações previstas, é necessário considerar a existência de excrementos de pássaros.

Palavras-chave: Energia solar e fotovoltaica, Medição de pó/sujidade em Painéis Fotovoltaicos, Análise de desempenho.

Contents

List of Tables

List of Figures

Nomenclature

E_{abs}	Absolute Error
AC	Alternating current
a-Si	Amorphous Silicon
E_G	Bandgap energy, (eV)
CdTe	Cadmium Telluride
CO_2	Carbon Dioxide
CIEMAT	Centro de Investigaciones Energéticas, Medioambientales y Tecnológicas
CMOS	Complementary Metal Oxide Semiconductor
CIGS	Copper Indium Gallium Diselenide
CF	Correction Factor
DLR	German Aerospace Center (German: Deutsches Zentrum für Luft-und Raumfahrt)
DHI	Diffuse Horizontal Irradiance, (W/m^2)
DSP	Digital Signal Processor
DC	Direct current
DNI	Direct Normal Irradiance (W/m^2)
DNI	Direct Normal Irradiance, (W/m^2)
GHI	Global Horizontal Irradiance, (W/m^2)
GNI	Global Normal Irradiance (W/m^2)
GTI	Global Tilted Irradiance (W/m^2)
JPEG	Joint Photographic Experts Group
Mono-Si	Monocrystalline Silicon
NTP	Network Time Protocol

V_{OC}	Open Circuit Voltage
PV	Photovoltaic
Poly-Si	Polycrystalline Silicon
P	Power (W)
RGB	Red, green and blue
E_{rel}	Relative Error
I_{SC}	Short Circuit Current
SL	Soiling Losses (%)
SR	Soiling Ratio
PSA	Solar Platform of Almería (Spanish: Plataforma Solar de Almería)
SAM	Sun and Aureole Measurement
UTC	Universal Time Coordinated

Chapter 1

Introduction

1.1 Role of Photovoltaic Technology to Climate Change

Climate change refers to long-term shifts in temperatures and weather patterns. These shifts may be natural, such as through variations in the solar cycle. However, since 1800, human activities have been the main driver of climate change, primarily due to burning fossil fuels, for example, coal, oil, and gas [1]. These activities are responsible for producing greenhouse gases, resulting in the rising of the Earth's temperature of about $1.1°C$ compared to the last 100 years. This may not seem a drastic change, but small variations in Earth's temperature can have adverse effects. Climate crisis can influence our health, ability to grow food, housing, safety, and work. Hence, there is an urgent need to shift our industry to clean, carbon dioxide (CO_2) emission-free [2].

Solar energy has experienced a remarkable growth and cost improvements over the past decade [3]. The reasons behind this increase in PV deployment lie in the several desirable advantages that PV technology offers [4]. One of them is the fact that it is widely accessible and easy to install and integrate into existing infrastructure. In addition, is a carbon-emission-free operation and has low operating costs. Also, the fact that is noise-free and operates at an ambient temperature, assures safety during the energy conversion process. Prices are declining rapidly and becoming increasingly competitive with fossil fuels all around the world [2, 5]. Despite the mobility and logistical challenges caused by the Covid-19 pandemic, renewable capacity additions increased by more than 46% from 2019 to 2020, breaking another record. With a record growth of 25% expansion of new solar PV installations to almost 135 GW [6]. PV generation increased 156 TWh (23%) in 2020 and reached 821 TWh. It demonstrated the second-largest absolute generation growth of all renewable technologies in 2020. Solar PV is becoming the lowest-cost option for electricity generation in most of the world, and is expected to propel investment in the coming years [4].

In addition to the climate benefits, solar energy provides a wide range of market and contributes to public health, including opportunities for job creation and economic development [2, 7]. However, PV technology has a few drawbacks, for instance, the low energy density, meaning that it requires large

areas. The initial installation costs and unpredictable output due to weather conditions are other disadvantages associated with PV technology. Thus, improvements in PV technology are needed, leading to a significant impact on sustainability, such as energy-efficient or addressing soiling problems.

1.2 Basic Functioning of a PV Device

This chapter gives an overview of how PV cell technology works. Essentially, a PV device delivers at its terminals electric power P, a flow *I* of electric charges with electric voltage, $P = VI$. DC can be fed directly to an energy storage device or to an inverter that converts it into AC. A PV cell is composed of a semiconductor material. When exposed to solar light, some photons are reflected, and others are absorbed by the material [7]. Semiconductors contain bonded electrons occupying an energy band called the valence band. In the same orbit electrons exhibit, different energy levels, and the grouping of these different energy levels is known as the energy band. If an incoming photon has enough energy (i.e. greater than a threshold called bandgap energy *Eg*), the electrons when excited moves to another energy band called the conduction band [8]. Figure 1.1 illustrates the operation of a silicon photovoltaic cell, which is the most common semiconductor material used in a solar cell [7].

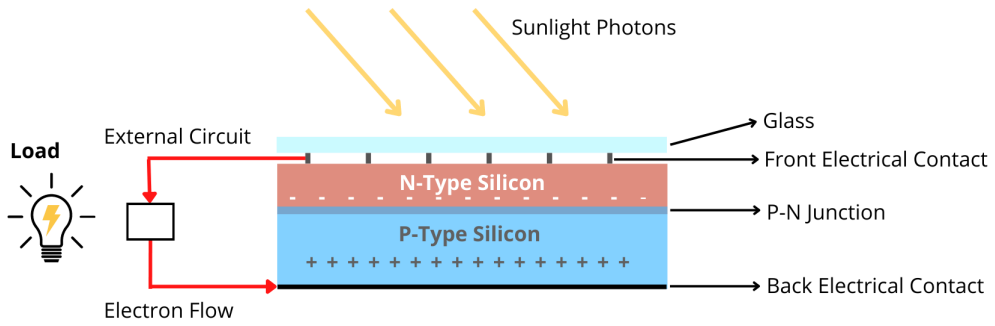

Figure 1.1: PV cell basic functioning.

Silicon solar cell. Positive field, p-type, and negative field, n-type. An imbalance of electrical charge results in voltage potential, providing energy in an external circuit.

This PV cell consists of two layers of semiconductor made of silicon, whose surfaces have gone through a special treatment, called doping treatment, to form an electric field to spatially separate generated charge carriers. This field is positive on one side (p-type, blue layer) and negative on the other (n-type, red layer) [6]. The photo-excited electrons by the sunlight photons move freely in the conduction band and the n-doped surface can collect them. The electrons lose their energy in an external circuit, that is, providing electricity (illustrated by the lamp) [8]. Later on, the electrons are restored to the solar cell by the return loop of the circuit entering in the p-doped layer, which returns electrons to the valence band with the same energy that started with. The electric potential when electrons are delivered to the external circuit is always less than the bandgap energy, even if the photons that created it had more energy. Thus the available electrical potential of a solar cell is essentially a characteristic of the material [8].

Historically, three different generations of solar panels can be distinguished [8]. The first generation is monocrystalline (mono-Si) and polycrystalline (poly-Si) silicon solar cells. The second-generation, thin-film solar cells, are made of amorphous silicon (a-Si), cadmium telluride (CdTe), or copper-indium-gallium diselenide (CIGS). Lastly, third generation, several emerging technologies including organic, quantum dot, perovskite, dye-sensitized solar cells, and others. Is worth mentioning, that multi-junction solar cells which have multiple p-n junctions made out of different semiconductor materials so that a wider range of bandgap energies is available for photon absorption [8]. Regarding the efficiency of solar energy technology, commercially available PV modules averaged less than 10% in the mid-1980s, reached 15% around 2015, and the efficiency is about 20% for state-of-the-art modules. According to the laws of thermodynamics, the maximum power conversion efficiency of a single junction, Si solar cell is 32.33%. This limit is based on the assumptions of perfect solar absorption and no losses due to non-radiative charge-carrier recombination. However, the maximum reached in a real-world case for silicon solar cells to date, achieved 26.7% conversion efficiency [9]. Experimental PV cells for niche markets, such as the space industry or research purposes have reached nearly 50% efficiency [8] The efficiency at which PV cells convert sunlight to electricity varies by the type of semiconductor material and PV cell technology [7].

1.3 Motivation

There is a growing interest in soiling mitigation on solar technology due to the significant impact on the maintenance and economics of solar energy plants. Since 2008, the publication rate on this topic has been increasing exponentially. However, the amount of research is small when compared to other fields in the solar power industry and research community, such as PV cell development [10, 11]. In that way, more research is necessary for the soiling department.

To make a well-founded decision as to when a PV panel must be cleaned, it is necessary to measure the soiling over a large area. This quantification (average degree of soiling) of the soiling would enable power plant operators to better plan optimized cleaning strategies within a solar field. Knowing the degree of soiling also enables a more accurate forecast of power plant performance [10, 12]. Soiling measurements are increasing in demand, as more and more power plants are being planned and built in desert regions with high dust loads. Therefore, accurate prediction and monitoring of soiling losses have become important. However, the soiling measurements commercially available are primarily local soiling sensors, covering only small areas [13]. Cameras are used with fully automated data acquisition. In this way, an entire solar field can be examined in a relatively short time and automatically evaluated via the recorded images.

A drone camera based in DLR (*Deutsches Zentrum für Luft- und Raumfahrt*, German aerospace Center) method is being developed to detect soiling on the PV modules and calculate how much it affects energy production. This method proved to be accurate and served as the foundation of this thesis. The objective of this project is to achieve similar accuracy results using a different camera, a

surveillance camera. Not only, a surveillance camera represents a cheaper cost compared to a drone camera, but also, allows one to store more data throughout the day. Lastly, it is flexible, meaning, it is not necessary to wait for good weather (e.g appropriate wind conditions) or to have prior knowledge of how to fly a drone.

1.4 Thesis Outline

In the context of this work, a novel measurement method is presented, which uses spatially resolved information from an image captured by a surveillance camera to derive statements about the degree of soiling of the PV modules. Firstly, the current state of the art is described. This includes soiling literature, highlighting important publications due to the relevance and uniqueness of the publication. In addition, a description of how soiling measurements were carried out in general and in power plants up to now. Afterward, the theoretical basics of solar irradiance concepts and knowledge about digital image processing are explained. Next, the camera-based method is described, and how a statement about soiling at a PV module can be made using an image recording. Data acquisition and the respective data processing and post-processing takes place. The final considerations are presented along with the insights that emerged from the evaluation of the camera-based method. Finally, conclusions and possible directions for future work are suggested.

1.5 Thesis Objectives

Given the previous context and challenges, it becomes obvious the advantages of monitorization and measurement of soiling on PV power plants. In this sense, the objective of the thesis here is to present a developed and effective non-intrusive methodology that is capable of estimating the soiling ratio with good accuracy using a digital camera. The program was initially developed by DLR (German Aerospace Center) for the drone-camera base method. This work presents another use of the same method but using a different camera, a static camera. The choice of the static camera used, the surveillance camera, has a reason. Firstly, the company DLR had already surveillance cameras ready to use. Secondly, PV parks are normally equipped with surveillance cameras for security reasons, and the method can be implemented afterward, having optimization of the use of the cameras without any effort. In that way, here are presented the objectives of this work:

- Determination of the soiling ratio on PV modules using a digital camera.
- Adapt the method developed for the drone camera to the surveillance camera.
- Calibrate the camera system and perform the necessary calibrations.
- Develop the Matlab code for the camera used.
- Performance analysis of PV modules under soiling conditions.

The work developed in this thesis, plus the collaboration with other authors, led to the contribution to the Conference PV Symposium 2023 [14], presenting ”Spatially resolved determination of the soiling of PV modules with surveillance cameras”.

Chapter 2

State of Art

The new century was marked by a growth in PV, both in research and in market. Hence, reflecting the investment in research funding reliability and expansion of installations worldwide. Soiling research and product developments shifted toward PV because of the rise in monitoring/measuring and country programs [15, 16]. This chapter starts by presenting a definition of soiling and how it distributes along the PV modules. An overview of the literature is given. Lastly, soiling measurements are discussed.

2.1 Soiling Distribution PV Module

Soiling in solar energy is the accumulation of snow, dust, leaves, pollen, and bird droppings on PV panels. Generally dust soiling is the term applied to solid particles with diameters smaller than 500 μm [11]. It occurs in the atmosphere from various sources such as dust lifted by the wind, pedestrian and vehicular movement, volcanic eruptions, and pollution. Distribution of soiling on the PV module is not homogeneous and depends on dust properties, environment, weather conditions, module properties, and its installation design [11, 17]. An important factor is the tilt angle of the solar panels [10, 5, 11]. Not only the effect of gravity on horizontal surfaces usually accumulates more dust than inclined ones but also results in a tendency for soiling particles to accumulate near the bottom of a PV module. On top of that, PV module frames can trap, in the bottom and side edges, particles or water runoff, enhancing the deposit of soiling, due to combined effects of gravity, precipitation, and wind [18].

Regarding the weather conditions, there are three determinants factors: wind, rain, and relative humidity. The wind carries the particles and deposits them onto the PV panel area, by attractive forces between particles. This natural agent can promote or demote dust accumulation, depending on the installation orientation, wind speed, wind direction, and dust properties. Generally, a low-speed wind pattern promotes dust settlement, while a high-speed wind regime has the opposite effect [10, 19]. Rain is quite effective at cleaning soiled surfaces if sufficiently abundant [10, 3]. However, rain can be considered advantageous and simultaneously deteriorative, as it can result in the deposition of a wet soiling. Few rainfall patterns normally promote better dust adhesion on panels. In fact, in the case of a severely dusted panel, a small amount of rain will turn dust into mud, attracting more dust [19].

Relative humidity and dew strongly enhance dust adhesion to surfaces through capillary forces, particle caking, and cementation. In the case of omitted cleaning, soiling can cause permanent degradation of PV modules, cemented dust layers, lichens, and fungi can become practically irremovable [10].

2.2 Literature Review

The literature stresses a strong interest and significance in studying PV soiling losses. However, there is a need to invest more money and time to address this externality. In the best places to deploy solar energy, dust is a problem [16, 17]. That is the case of MENA (the Middle East and North Africa) and desert regions. This chapter presents several key review papers covering this topic, which provide the source authors, the publication year, a summary of the review contribution and focus, and the solar technology covered. Soiling rates occur at various rates in different parts of the world. Therefore, it is difficult to generalize the conclusions observed in scientific papers. In that way, literature presents contradictory results and misleading conclusions [16].

The initial period includes contributions from the solar pioneers Hottel and Woertz, Tomlinson, [15] who investigated the impact of dust accumulation on solar systems. Garg (1974) (India) [20] study concurred with the fact that horizontal glass receives more dirt than vertical one. Transmittance values after sun exposure for horizontal and vertical PV, were found to be 30% and 88%, respectively. A significant conclusion from the study revealed only an 8% reduction in transmittance for a 45-tilted glass plate after a month. A relevant article conducted by Nahar and Gupta (1999) (India) [15] in a desert environment in Thar, India, was the impact of dust on the transmittance of various glazing materials. The reduction in transmittance appeared different for distinct materials and different tilt angles. Concluded that, solar panels subjected to desert conditions should be cleaned daily [11].

Research after the 1990s, can be characterized by an integrated nature of investigation augmented with sophistication in experimental rigor resulting in better reliability and accuracy [11]. Mohammad and Fahmy (1993) [20] studied the effect of the physical properties of dust (mainly particle size), and the influence of the amount of dust on the output of a solar panel. Their work showed that smaller particles have a far greater effect than larger particles on the transmittance of glass. Goossens et al. (1993) [21] studied the effect of wind speed on the deposition of dust in Israel. Results showed that even the slightest turbulence in the atmosphere affects the movement of dust particles due to extremely small inertia and under all wind directions, indicating a general increase in dust deposition with an increase in wind speed [11]. Adel (2001) and Hassan et al. (2005) [20] came to a similar conclusion: the speed of decrease in transmittance decreases with time and reaches a saturation point after 30 days of exposure. Elminir et al. (2006) (Egypt) [22] used 100 glass panels with different tilt angles and measured a dust deposition of $15.84 g/m^2$ ($0°$) and $4.48 g/m^2$ ($90°$). Ransome and Sutterlueti (2012) [23] modelled a linear increase in the losses in Madrid (Spain) and how the soiling behavior dominates the cost in regions with long periods without rainfall. Pavan et al. (2011) [24] determined in Italy that the influence of soiling was higher for a 1 MW PV power plant on sandy soil, with 6.9% annual losses, compared to an annual loss

of 1.1% for compact soil [20]. Andrews and Pearce (2012) [25] developed a methodology for predicting losses based on readily available meteorological data, especially for snowfall.

An extensive part of soiling research is concerned with the effect of dust or soiling at various locations in the world. This information plays a meaningful role in collaboration among researchers and developers to address the issues of soiling and mitigation, assisting in better site location and operation and maintenance costs for the PV systems [11]. The publications also indicate some trends toward these concerns with mitigation [15]. So far, no passive anti-soiling technology (e.g., surface coatings) eliminates the need for cleaning. Moreover, there is not a universally recommended cleaning method, as the economics and effectiveness change with local conditions, available resources, and cleaning frequencies. Research on this aspect is lacking, suggesting that more investigation is needed on soiling monitoring, soiling modeling, and integration into meteorological models [10].

2.3 Soiling Measurements

This section describes current methods for measuring soiling in solar fields. First, different soiling measuring devices are presented. Afterward, a drone camera-based method for the detection of soiling developed in the DLR will be presented, which is the origin of this work.

Since a few years, sensors for integration into the solar field have been available, which determine the soiling on a small measuring area ($< 100cm^2$) [13, 26]. Another soiling measurement typically used is a pair of PV reference devices, one PV module is continuously clean and the other is naturally soiled. The soiling losses are determined by comparing the output of the soiled reference device with the output of the clean one. The clean reference device may be either a reference cell or another PV module [18]. Afterward, a study conducted by [27] concluded that measurements should be restricted to the middle portion of the day. Thus, excluding high uncertainties from morning and evening hours related to lower signal amplitudes and the effects of angular alignment differences, preferably averaging data for equal periods around the solar noon. Another effect that must be considered, is that moving clouds may cause the irradiance received to differ between modules. In addition, using PV modules as a reference allows the effect of soiling in the real world to be measured, capturing soiling patterns that may not be replicated by smaller work-pieces such as PV cells or glass coupons [28].

One problem with the methods described is the small area covered that is measured in comparison to the solar field. Furthermore, the soiling behavior on the surface of fixed sensors is not necessarily the same as that on the PV panels [13].

There are already publications on the subject of camera-based soiling detection [29]. One article presents a method for quantifying the amount of dust on PV modules by investigating five different image processing techniques. This study deals with the analysis of color histograms and statistical properties of the captured images of PV modules. An image processing toolbox has been developed using the following techniques: Binarization, Histogram Model, Statistical method, Image Matching, and

Texture Matching [28, 29]. In another study, PV module images taken by a camera under laboratory conditions for different dust accumulations detected different features of the gray-level cooperation matrix. The obtained data with new features are classified based on artificial neural networks to determine the dust load and its influence on PV module performance [30]. However, the approaches listed have all so far only been tested under laboratory conditions and are still far from large-scale application or commercialization.

DLR already has a measurement approach that uses a drone camera to make automated and rapid measurements of a large number of PV modules under real operating conditions. Since the measurement method and software were developed at DLR, knowledge and technology can already be drawn on. When taking images with the drone, the 3D PV module geometry can be determined in the millimeter range. The panels are automatically identified and segmented. After segmentation, an orthographic image of the PV panel is generated using various algorithms. In addition to the position and geometry, the position of the drone and the viewing direction of the camera as well as the position of the sun, are known. The entire information is read out after the flight with the help of the software and can be used for further calculations [31, 32]. To capture the optimal images, automatic flight route planning is used, in which the recording parameters can also be set. Thus, flight routes can be planned in which the angle between the sun and the camera is optimal. For almost all projects, knowledge of the sun position is a prerequisite. Also relevant experience was gained from other developed projects that evaluate the light intensity of a camera, such as a cloud determination or sun shape measurements with SAM (sun and aureole measurement).

Chapter 3

Fundamentals

Basic definitions of solar irradiance concepts, angle definition, and the nature of a camera image are discussed.

3.1 Solar Irradiance Concepts

As solar photons travel through the atmosphere, a significant amount of energy it is attenuated, partially the radiation is absorbed by the atmosphere or scattered, for example, deposited dust hence scattering behavior or absorption. Solar radiation concepts are introduced to distinguish all the solar components [8, 19, 33, 34].

Solar radiation (W) is the radiant energy emitted from the sun. Irradiance refers to the amount of solar radiation obtained per unit area by a given surface (W/m^2)

Direct Radiation is the solar radiation received from the sun without having been scattered by the atmosphere (W).

Diffuse Radiation is solar radiation that does not arrive on a direct path from the sun due to scattering by the atmosphere. Global solar radiation is the sum of the beam and the diffuse solar radiation on a surface (W).

Irradiance (W/m^2) is the rate at which radiant energy is incident on a surface per unit area of the surface. The symbol G is used for solar irradiance, with appropriate subscripts, for example, direct and diffuse radiation. The solar irradiance intensity depends, among other things, upon the solar elevation angle. This is measured horizontally. When the solar altitude is perpendicular to Earth, the sunlight takes the shortest path through Earth's atmosphere. But if the sun is at a flatter angle, the path through the atmosphere is longer. This results in greater absorption and scattering of solar radiation and lowers radiation intensity.

Spectral irradiance is the irradiance of a surface per unit frequency or wavelength.

Direct Normal Irradiance (DNI) is the solar radiation that comes in a straight line from the direction

of the sun received per unit area by a perpendicular surface (W/m^2).

Diffuse Horizontal Irradiance (DHI) represents solar radiation per unit area that does not arrive on a direct path from the sun (W/m^2).

Global Horizontal Irradiance (GHI) is the total irradiance from the sun on a horizontal plane (W/m^2).

Global Normal Irradiance (GNI) is the total irradiance from the sun at the surface of Earth at a given location with a surface element perpendicular to the Sun (W/m^2).

Global Tilted Irradiance (GTI) is the total radiation received on a surface, for example, a PV panel with defined tilt and azimuth angle, and can be modeled from GHI, DNI and DHI (W/m^2).

3.2 Angles Definitions

Exact knowledge of the sun's path and angles is essential for calculating irradiance values and the yields of solar energy systems. Figure 3.1 presents an overview of relevant angles for the understanding of solar energy and is also used in this project.

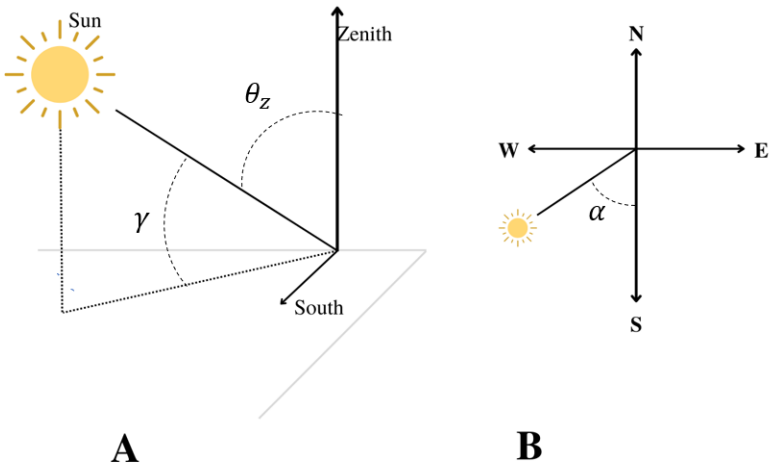

Figure 3.1: Sun position angles definition.
(A) θ_z zenith angle, γ . (B) Plan view showing solar azimuth angle, α.

Zenith angle θ_z, is the angle between the vertical and the line to the sun. Solar altitude angle, γ, is the angle between the horizontal and the line to the sun, that is, the complement of the zenith angle. On the left, Figure 3.1 B, solar azimuth angle, α, the angular displacement from south of the projection of beam radiation on the horizontal plane [33].

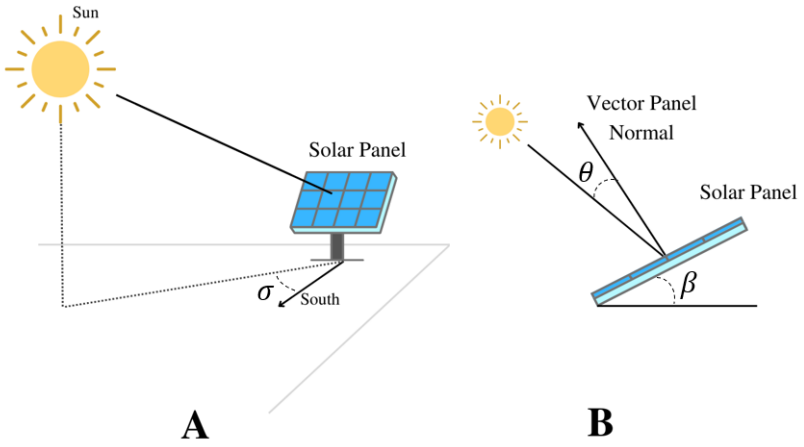

Figure 3.2: Panel position angles definition.
(A) σ PV panel azimuth. (B) θ incidence angle; β slope angle.

On one hand, in figure 3.2 A represents the angle between the solar panel orientation and the position of the sun is depicted σ, panel azimuth. On the other hand, in figure 3.2 B, it is possible to observe the angle of incidence θ, the angle between the beam radiation on a surface and the normal to that surface The slope, also called the tilt angle of the PV module, the angle between the plane of the surface in question and the horizontal, $0° \leq \beta \leq 180°$. During the experiments, this angle was equal to 30° for all the modules under study. The optimum angle refers to the angle at which solar PV modules should be oriented to generate maximum electricity [33].

3.3 Solar Cell I–V Characteristics

The operation of a solar cell can be defined by the relationship of the current-voltage (IV) curve. Figure 3.3 illustrates a characteristic solar cell IV curve. The typical operational state is the maximum power point (MPP), which is found by maximizing the product of the current (I_{MPP}) and voltage (V_{MPP}), $P_{MPP} = I_{MPP} \cdot V_{MPP}$ (is measured in Watts, *W*, or Watts peak, *Wp*). Thus, if all solar cells are operated at this point, the maximum energy generated by a PV module can be achieved. Ensuring the operational state at MPP is an optimization problem, which is technically solved by maximum power point tracking (MPPT), where a controller follows an algorithm adjusting operational states frequently by the means of comparing and maximizing power levels. Other important parameters are the open circuit voltage (V_{OC}) and short circuit current (I_{SC}). Open-circuit voltage is the maximum voltage that PV provides when the terminals are not connected to any load. Short-circuit current, is an over current resulting from a short circuit and is the maximum current provided by the PV. The fill factor, FF, is the fraction between the maximum power (P_{MPP}) conditions and the product of the open-circuit voltage and the short-circuit current ($V_{OC} \cdot I_{SC}$). It is the ratio of the areas of the two rectangles and is always less than one. Thus, the closer this FF value is to one, the more power can generate. Lastly, the efficiency of

the PV module is the ratio between the power the PV can produce at MPP conditions and the incident power, P_{in}, which is determined by the properties of the light spectrum incident upon the solar cell. [8]. Further information regarding the experimental determination of the PV panels' efficiency appears in chapter 4.4.3.

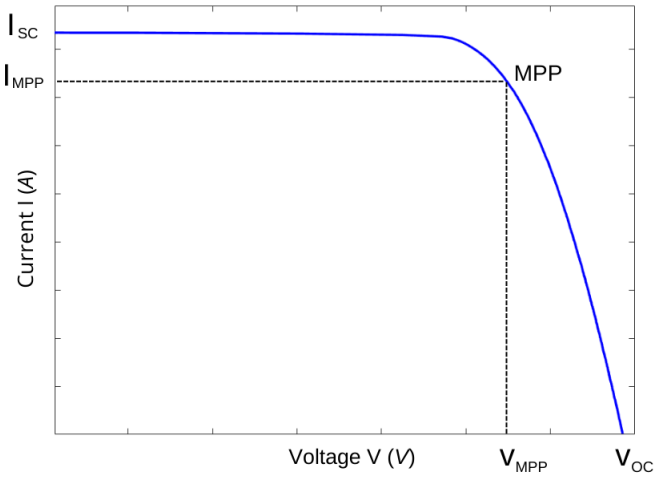

Figure 3.3: Solar cell IV characteristic curve.

Current-voltage (IV) graphic. Maximum power point (MPP), the product of V_{MP} and I_{MP}. Short-circuit current, I_{SC}. Voltage in open-circuit, V_{OC}.

3.4 Image Processing

Digital image processing is the computational manipulation of an image to enhance the image quality or to extract information. The scientific and economic value of this field led to many contributions during the last decades, which resulted in a massive variety of image tools. It is important to know more about field-specific terms and how an image is digitally coded and decoded [35].

3.4.1 Images as Matrices

Digital image representations do not depict continuous color gradients but a finite number of uncolored elements called pixels. In computer science, images are saved as matrices, with each entry of the matrix containing the color information pixel. The way the information is interpreted is specified by color space. Depending on the application, using different color spaces might be more useful and/or meaningful. Only RGB (color space) image representations were used in this project. This encoding concept is based on the Young-Helmholtz theory of the trichromatic color visions of humans. According to this theory, the human eye is only able to use the information of three basic colors: red, green, and blue [36]. The interpretation of the ratio of all three colors represents the entire spectrum of colors the human eye experience in daily life. Captured images are saved and divided into individual pixels. Each pixel consists of three layers and is composed of a red, green and blue value, figure 3.4. Each of these

color values can have an RGB value between 0 and 255. The absolute values of the red, green and blue RGB values are used to compose the color of the image.

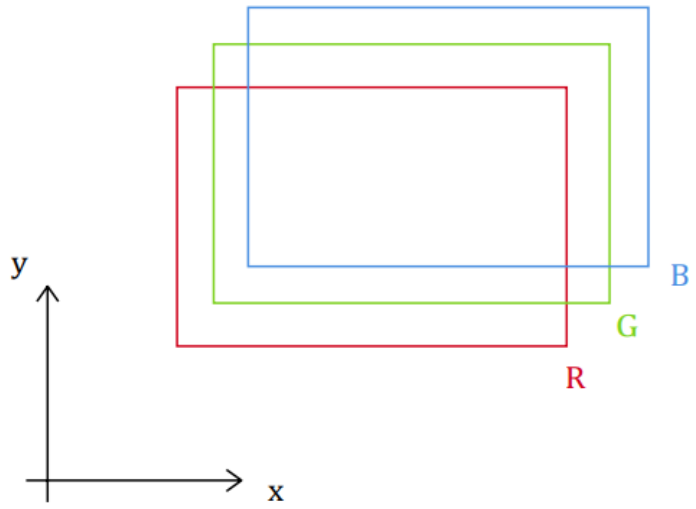

Figure 3.4: Pixel RGB image.
Each pixel consists of a red, green and blue value.

Thus, a pixel comprises three subpixels, each subpixel able to display one of the elemental colors with 256 different intensity levels. Therefore data is stored in three different matrices [35].

3.4.2 Image Type

For further calculations, two image types were used: grayscale image and binary image (also called masks). Both image types have a significant role throughout of development of this thesis.

The grayscale image depicts an image of class unsigned-integer with 256 different grayscale levels and can be regarded as an illustration of intensity levels. With the different three matrices from the RGB discussed previously, can display three distinct greyscale images due to their intensity differences in the channel.

The binary image contains only two states: zero (black) and one (white). This was very useful to create a ignore mask in chapter 4.3.1 and for the segmentation of cell orthoimages. A global thresholding method was used, which requires creating a histogram, defining the threshold, and apply. Based on the histogram information, a particular greyscale value is calculated. After defining the interval of the pixel value (0 to 255), all pixels with grayscale values below or above the threshold are tagged as true or false. Lastly, convert values of pixels tagged as false to 0 (black) and pixels tagged as true to 1 (white).

Chapter 4

Methodology

4.1 Camera-Based Method Principles

The theoretical basics for the detection of soiling in solar panels through the camera image evaluation are clarified and shown.

4.1.1 Pixel Values to Irradiances

Several mathematical operations are conducted between the CMOS (Complementary Metal Oxide Semiconductor) sensor pixel signals and the resulting image [37]. To derive irradiance values, these operations must be partially reversed. A spectral irradiance E_λ falling on a pixel's surface (dA) during the exposure time (t_{exp}) creates the raw signals of the CMOS sensor's pixel. The three signals corresponding to the three color RGB filters are weighted with the camera and color-dependent spectral responsivity written as ϵ_{nm} and also weighted with a camera-specific 3x3 matrix M_{cam}. Afterward, if there is one, the gamma correction Γ_{sRGB} is applied. The gamma correction is a nonlinear operation adjusting the physical photonic measurements to human perception, explained in detail in section 4.3.1. Depending on the camera and settings, an offset ($\vec{offset}$) must be added. The value of a pixel is thus defined by Equation 4.1 [38].

$$\vec{S_{sRGB,mn}} = \Gamma_{sRGB} \cdot (\int_{A_{mn}} \int_{\lambda_{min}}^{\lambda_{max}} t_{exp} \cdot \vec{\epsilon_{nm}} \cdot E_\lambda d\lambda dA + \vec{offset}) \tag{4.1}$$

A_{mn} is the area of the pixel *mn*. The pixel (*mn*) of the RGB image with the three color channels RGB is represented by $\vec{S_{sRGB,mn}}$. λ_{min} and λ_{max} are the minimum and maximum wavelengths of the broadband spectrum, respectively. E_λ denotes the irradiance with wavelengths $\lambda \pm d\lambda$ on sensor area dA before entering the camera. t_{exp} is the exposure time of the camera, which is constant.

In this project, the used camera system is a standard surveillance camera, described in section 4.2.1, and the gamma correction applied by the manufacturer is intentionally removed. In addition, each pixel is normalized into the interval [0,1] and converted to grayscale. The grayscale conversion, the normalized color channels, and the weighting factor for each color channel were done according to P. Kuhn (2017)

[38], which used the same camera for his work. The weighting factor for each color channel is calculated from Planck's law [38], and the chosen white balance temperature (10000 K). Thus, the weights of the camera-specific matrix M_{cam} can be reversed. Moreover, the offset term was photometrically measured and was found to be neglectable [38, 37], resulting in the transformed equation 4.2.

$$S'_{mn} = \beta_{\vec{Planck}} \int_{A_{mn}} \int_{\lambda_{min}}^{\lambda_{max}} t_{exp} \epsilon_{\vec{nm}} \cdot E_\lambda d\lambda dA \tag{4.2}$$

Three further assumptions were made. Firstly, the distribution of the spectral irradiance E_λ is assumed to be homogeneous for the area of each pixel. Thus, the integral over the pixel area A_{mn} is replaced by a constant. Secondly, ϵ_{mn} can be different for every pixel but is assumed to be constant over the area of a given pixel (dA) and the considered wavelength spectrum. Thirdly, the broadband irradiance is defined as the weighted integral of E_λ from 280 *mn* to 4000 *mn* as specified in Gueymard and Vignola (1998) [39]. With these assumptions and the gamma correction undone, there is a linear relation between the broadband (BB) irradiance $E_{BB,mn}$ and the value of pixel (*mn*) in the linearized grey image S' [38].

$$S'_{mn} = const_{mn} \cdot E_{BB,mn} \tag{4.3}$$

4.1.2 Optical Effect of Soiling

Generally, PV modules appear brighter when soiled. Figure 4.1, is possible to distinguish the cleaned from the soiled module. This assumption is based on the fact that the dirt layer on a PV panel, which depends on the optical properties (size, shape, reflectivity), scatters part of the incident light. The more particles there are per module surface, the more light is scattered, assuming constant illumination conditions. Part of the scattered light is directed toward the surveillance camera, contributing to the pixel RGB value, appearing the PV soiled panel brighter.

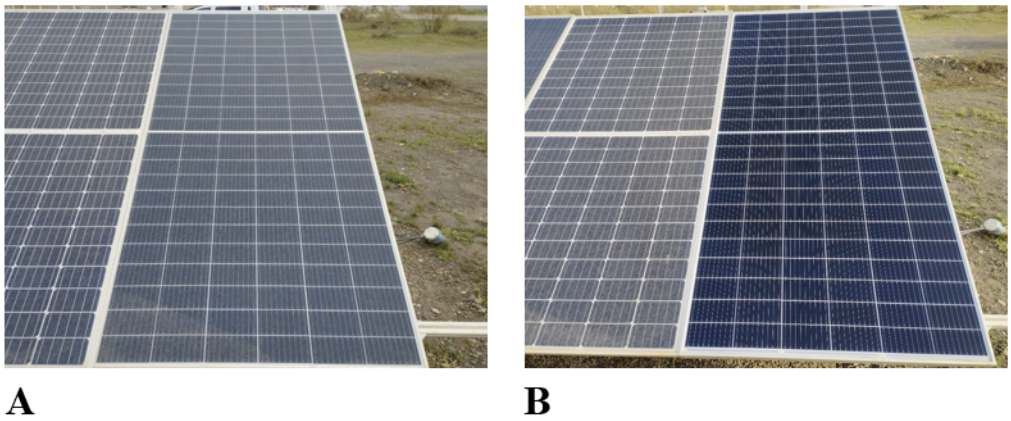

Figure 4.1: Before and after cleaning the PV module.

(A) Soiled PV module. (B) Cleaned PV module. The optical effect of soiling on the PV soiled panel appears brighter, while the PV cleaned panel presents a dark blue color.

In the case of scattering by particles, both the particle number size distribution and the solar spectrum of the sun play an important role. In addition to scattering, the internal settings of the camera should be taken into account when taking images. Manufacturer corrections make it difficult to compare the images with each other. Thus, the effects of gamma correction and vignetting are examined in chapter 4.3.1 for the respective camera. In addition, for the same conditions of soiled conditions, depending on the sun and viewing position, the brightness can appear different in the modules. Normally, PV modules appear brighter when viewed from the side. This effect is significantly important for the camera-based methods, due to their variability in sun and camera positions during the recordings, meaning that the brightness of the PV module can be different depending on these two parameters.

Part of the sun radiation that reaches the PV panel is scattered, other is absorbed by the particles or material, and part of the radiation passes through, which is called transmission. The scattering in the direction of surveillance cameras is used to detect the soiling on the PV module. Thus, the RGB image captured value is analyzed pixel by pixel from the corresponding image. Aforementioned in the previous section, the camera has a sensor whose RGB value is proportional to the radiation reaching the pixel sensor, shown in the equation 4.3 if a few conditions are verified. In addition, the evaluations were conducted on the greyscale image of the red color channel due to the high contrast. This assumption was made based on the fact that PV panels are blue and there is green vegetation around the PV setup. As a consequence, the red color channel shows high contrast, which positively affects the method.

During the camera recordings, it measures the reflections at the module surface, the background of the cell, and the scattering due to the soiling layer (Mie-scattering). The equation 4.1.2 defines that the irradiance from a soiled module is the sum of the irradiance from a clean module plus an additional scattering term.

$$E_{soiled} = E_{clean} \cdot \tau_{soiling}(\alpha_{sun}) \cdot \tau_{soiling}(\alpha_{camera}) + c_{scat}(\vec{r_{sun}}, \vec{r_{camera}}) \cdot E_{scat}(\tau_{soiling})$$

(4.4)

E_{soiled} is the radiation reaching the camera from a soiled module. The radiation that would reach the camera sensor if a certain module was cleaned is E_{clean}. The $\tau_{soiling}$ is the optical transmittance of the soiling layer, which is dependent on the sun and camera position. The relative angles α_{sun} and α_{camera} are the angles between the PV panel normal and sun, and the angle between the PV panel normal and camera, respectively. c_{scat} is an empirical function to describe the scattering behavior of the soiling layer in dependence on the sun position and the camera position. Finally, the light scattered at the soiling layer is characterized as E_{scat}, which is dependent on the soiling losses.

This equation was developed by the drone-camera-based method and the main objective of this thesis is to adapt all the variables to the static-camera case, to solve this equation. Overall, the terms of the equation, in the end, were determined or given by the captured image itself, except $\tau_{soiling}$, the

soiling losses. In the beginning, only the initial term, E_{soiled}, is known from the captured image, the total radiation coming from a soiled module to the camera. The following terms were calculated. From the data acquisition, the sun and camera vectors as the respective angles were discovered. Moreover, in chapter 4.4.2 the calibrations takes place, named scattering and clean calibrations, to determine the empirical function, c_{scat}, that describes the scattering light on the soiled module and the radiation of a clean module E_{clean}. Lastly, the scattered radiation, E_{scat}, that reaches the camera is dependent on the $\tau_{soiling}$.

In the following chapters, data acquisition and data processing are introduced to determine resolved images and know the contribution of the RGB value of the image captured to calculate the soiling losses.

4.2 Data Acquisition

This section gives an overview of the surveillance cameras used in the Solar Platform PSA (Plataforma Solar de Almería)and the relevant settings defined in the camera system. Figure 4.2 illustrates a simple drawing of the PV set up in the desert Tabernas Almería. Overall there are twelve modules in the PV setup, but only the four modules in the center are evaluated in this thesis due to the technology's compatibility. Each module has an ID number from 1 to 4, as illustrated in the image. On one hand, the right side of the PV setup is cleaned every day, meaning that modules 2 and 4 are cleaned. On the other hand, modules 1 and 3 are naturally soiled. This layout configuration is fundamental in this work, along with the electrical power output of all modules in the center, to calculate the electrical output reference. The four modules have the same technology and are from the same manufacturer. The only difference is the cell type: modules 1 and 2 have 60 cells; modules 3 and 4 have 72 cells. For all the processes and computation, number identification is used as described in figure 4.2.

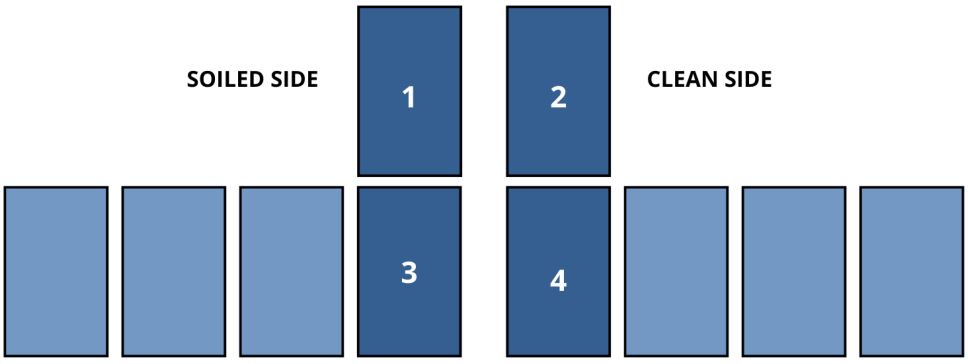

Figure 4.2: PV setup, layout configuration .
Four under-study PV modules are in the center of the setup. ID number from 1 to 4.

This layout configuration not only plays an important role in calculating the electrical output reference with the module comparison method, chapter 4.4.3, but also is essential to perform the clean and scattering calibration, discussed later in chapter 4.4.2. In figure 4.3, is a raw image from the surveillance

camera perspective tagged with the following layout described previously. Apart from the description of the modules is also possible to spot pyranometers near the modules, mentioned in the next section.

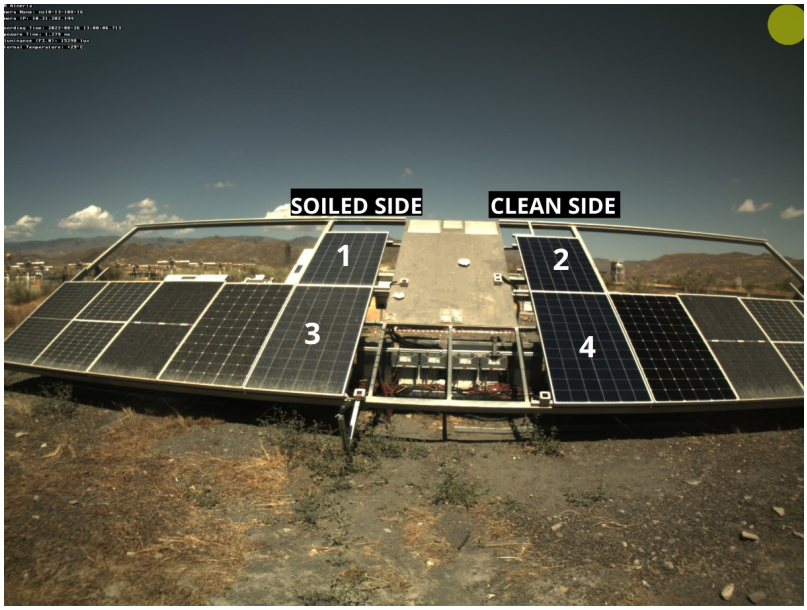

Figure 4.3: PV setup, surveillance camera captured image. August 26^{th}, 1pm UTC+1.
Four under-study PV modules are in the center of the setup. ID number from 1 to 4.

4.2.1 Surveillance Cameras

In this project, the cameras used are off-the-shelf standard surveillance cameras (Mobotix MXM24M-Sec-D22, CMOS sensor) [40]. The surveillance camera used in this project is depicted in figure 4.4.

Figure 4.4: Surveillance camera.
Mobotix MXM24M-Sec-D22, CMOS sensor [40].

This project has been developed in Plataforma Solar de Almería (PSA) in the Tabernas Desert in the south of Spain. Scientists from CIEMAT (Centro de Investigaciones Energéticas, Medioambientales y Tecnológicas) and DLR (German Aerospace Centre) operate several meteorological measurement stations, including all-sky images, pyranometers, pyrheliometers, and more recently surveillance cameras to measure solar energy concepts to bring novelty results and replace costly measurement equipment or even to increase the efficiency of the current equipment [38].

The first time that the camera system was established in DLR was in 2014. Then, it was upgraded in 2015 and dismantled again in 2018 [38]. At the moment, six surveillance cameras are dispersed to various projects with different purposes. For this project, there is one dedicated camera, called shadow 1, recording the PV setup located 5 meters away that oversees the majority of the modules.

Additionally, the shadow camera system can have access to data from a grid of 20 Si-pyranometer (Apogee SP Series, LICOR LI200 SL, and Kipp Zonen Split; GHI measurements) described in Schenk et al. (2015), three tracked pyrheliometers (Kipp Zonen CHP1; DNI measurements) and three shadow ball shaded pyranometers (Kipp Zonen CMP21; diffuse horizontal irradiance (DHI) measurements). All data acquisition systems are synchronized via an NTP server [38].

4.2.2 Camera Settings

Several factors can influence the path of the radiation to the lens up to the digital image value. These include the aperture and the shutter speed, which were kept constant during image acquisition to avoid possible influences, making the images comparable. When the images are stored in the more common JPEG format, the camera's digital signal processor (DSP) next performs Bayer pattern [41]. Sharpening is also often applied at this stage. Subsequently, the color values are multiplied by various constants to perform a white balance. Finally, a standard gamma function is applied to the intensities in each color channel before being compressed into JPEG format [42]. In that way, camera settings have been empirically determined once and retained for each recording. This includes, for example, image quality, contrast, and white balance. Automated adjustments recording correction programs that come from the manufacturer have been turned off, ensuring that the images are as realistic as possible and can be compared.

An important setting to be defined is the distance between two shots, i.e time interval between images. After the recordings tests, the time interval was set to 60 seconds due to the variability of the clouds that influence the output. One of the main challenges was to define a fixed exposure time since the brightness changes during the day and according to different meteorological conditions. The fixed exposure time used was 1280 microseconds, which is the most suitable for the local conditions. Table 4.1 presents the settings defined in the used camera.

Table 4.1: Surveillance camera settings.

Surveillance Camera Settings	
Image Size	QXGA(2048x1536)
Image Quality	High
Frames per Second	4fps
Exposure Time	1280 ms
Time interval	60s
White Balance	1000K
Automatic Contrast	Off
Brightness	0
Backlight Correction	0
Noise Suppress	0

4.3 Data Processing

Every camera lens introduces distortions in the image. One feature widely used in surveillance cameras is the fisheye effect or super-wide angle. In this case, the camera used has super-wide angle lens (22mm, 90°, F 2.0) [40]. The main characteristics of these lenses are the radial and tangential distortions. These distortions increase from the center to the edges of the image. Therefore, the amount of correction to be applied should also vary accordingly, based on the pixel location. On top of that, every lens causes a vignetting effect, which is a darkening of the corners and edges of the image [43].

The methodology to derive resolved images is presented in detail in this chapter. The objective after the data acquisition is to evaluate the gamma correction and normalize the vignetting effect. In that way, making the images as true to life as possible. Afterward, it is necessary to remove the distortion caused by the lens and create orthoimages of the modules. Later, a mask is applied and cell orthoimages are generated.

4.3.1 Image Corrections

Despite all the settings set in the camera systems, every lens and camera introduce effects in the digital imaging [44]. Hence, influencing the soiling evaluation if not corrected.

Gamma Correction

One problem with capturing images is the difference between physical and human perception. The physical perception of the camera sensor is linear. The more light that hits the camera lens and thus the camera sensor, the higher the measured brightness or voltage at the sensor. Human perception, on the other hand, is not linear. Compared to a camera, the human eye is much more sensitive to

changes in dark tones than to similar changes in light tones. Thus, allowing human vision to work over a wider range of luminance. Otherwise, the typical range of brightness encountered outdoors would be too overwhelming. Precisely the gamma correction is a function that relates the pixel's numerical value and it is actual luminance, to compensate for the non-linear luminance effect [44], equation 4.5.

$$g(x) = f(x)^{\frac{1}{\gamma}} \tag{4.5}$$

For this reason, an attempt is made to reverse the gamma function applied to the images. This is done with the inverse function of the gamma function, equation 4.6.

$$f(x) = g(x)^{\gamma} \tag{4.6}$$

To obtain the gamma function experimentally, the same subject was photographed with different exposure times. Some of the images with the corresponding exposure times in microseconds (ms) are shown in figure 4.5. The longer the exposure time, the more light hits the lens and the image becomes correspondingly brighter. For faithful reproduction of the images, the gamma value should be ideally equal to 1, this has been investigated in various publications [44, 45]. Based on this knowledge, the gamma function can be determined experimentally by varying the exposure time.

Figure 4.5: Gamma experiment, captured images.
Three different exposure time images for the gamma experiment in microseconds (ms): 320ms; 640ms; 1280ms.

After running the gamma evaluation, it was found that for exposure times higher than 640 microseconds the relationship of the three color channels between the two images with different exposure times, was linear, that is, gamma is equal to 1, figure 4.6. That is a confirmation that all the settings from the manufacturer are turned off and is not necessary to apply any gamma correction since this project only worked with higher exposure times. However, for lower or dynamic exposure it might be important to take care of this correction before going to the soiling analysis, since the system gamma is slightly greater than 1 to improve contrast. Additionally, in the graphic in figure 4.6, it is possible to observe that for a pixel value higher than 160 it might have some effect causing a systematic deviation in the output. Thus, for heavy soiling, the brightness of the module is higher, and perhaps is necessary to correct the gamma function. In this case, none of the values seen in the data acquisition was higher, so no gamma correction was applied during the project.

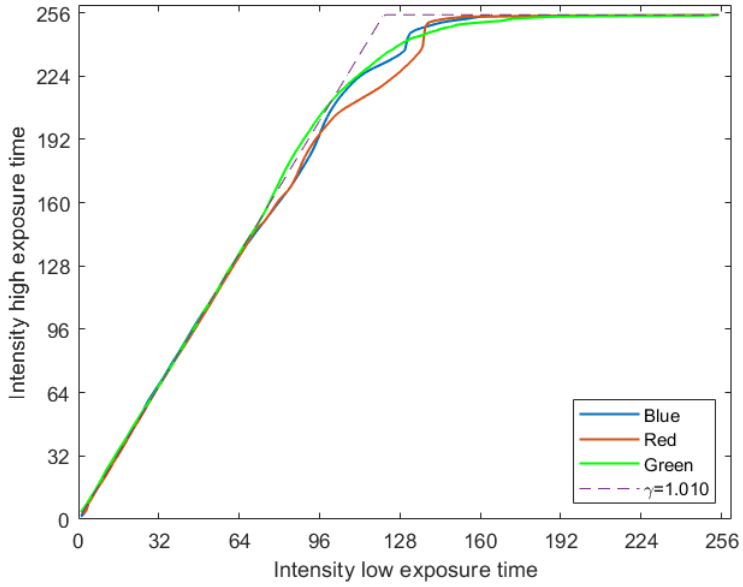

Figure 4.6: Gamma experiment evaluation graphic.

Relationship of the different color channels, RGB, from 0 to 255 intensities, between an image with high exposure time (y-axis) and an image with low exposure time (x-axis).

Vignetting Correction

In photography, it is common to have a darkening of image corners when compared to the center. This optical effect, called vignetting, occurs in all lenses, and depending on the optical design and construction of the lens, it can be quite strong. It is more notable in lenses with large apertures or barrels, since light is entering the camera can be blocked by the barrel. As a result, the light that reaches the image plane at such angles naturally falls off (decreases in brightness) towards the extreme corners of the frame. Thus, wide-angle lenses increase the vignetting effect, as the light takes longer to travel from the edge of the lens to the center [43] .

This calibration was carried out by measurements with an integrating sphere. The integrating sphere is held in front of the camera lens so that the interior of the integrating sphere is recorded when taking a picture. The light inside the sphere is homogenized by scattering on the inner surfaces. The heterogeneous irradiance recorded by the camera sensor is caused by the attenuation of the camera. However, there were complications to fit the camera inside the integrating sphere due to the protection cape of the camera. Despite all the efforts, the image did not cover the desired area from the integrating sphere. In figure 4.7 A is possible to see one image from this measurement. To overcome this issue, a mask, figure 4.7 B, was created during this calibration, identifying: the darker pixels from the borders (range of pixel value 0 to 100); the brighter pixels values, around 255 due to the light source; the yellow dote (recording symbol from the camera system) and the text box located in the upper left corner. In the end, the vignetting evaluation was obtained considering only the pixel values from the integrating sphere, i.e the part not masked in figure 4.7 B.

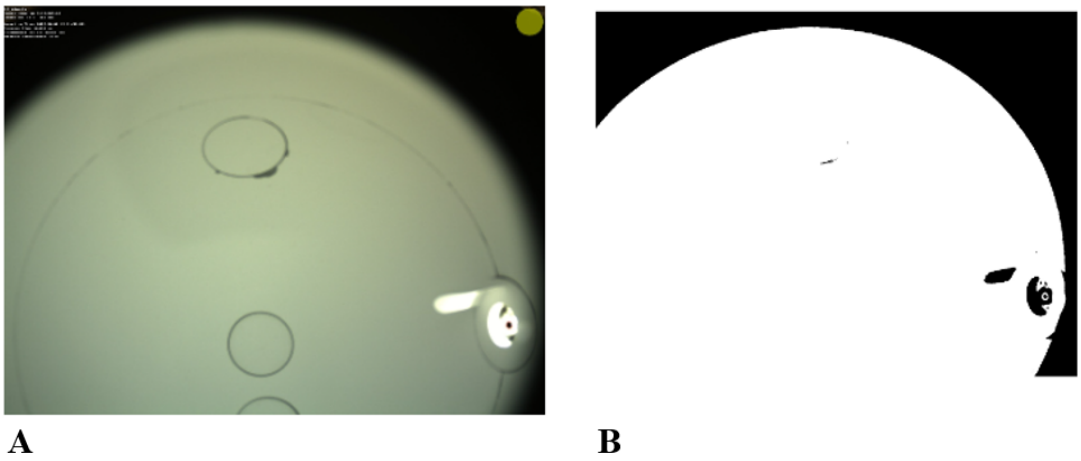

Figure 4.7: Integrating sphere captured image and ignore mask.

(A) Integrating sphere captured image by the surveillance camera. (B) Ignore mask. The solution to overcome the fit problem between the camera and the integrating sphere.

Figure 4.8 shows the captured normalized vignetting matrix. Afterward, this Vignetting matrix was applied to every image taken for the evaluation. Due to the fit between the camera and the integrating sphere, there is a systematic deviation in the upper part of the matrix. Nevertheless, this was found to be irrelevant, since the upper part of the image taken by the camera is not used because the PV modules are located in the middle of the image.

Figure 4.8: Vignetting matrix.

Obtained normalized [0 1] vignetting matrix excluding the pixel values from the ignore mask.

4.3.2 System Calibration

If the entire system is considered calibrated, it means that the camera calibration and camera orientation are simultaneously satisfied. Camera calibration is the process of determining the interior orientation parameters [46]. Interior orientation determines the camera's deviation from an ideal one-point perspective model. Deviations arise, for example, from non-ideal lenses and effects on the iris. The parameters to be found by the camera calibration depend on the type of camera used. Camera orientation usually includes the determination of the parameters of exterior orientation to define the camera station and camera axis in the higher-order object coordinate system, frequently called the world coordinate system. This requires the determination of three rotational and three translational parameters, in a total of six parameters [46]. Two methods were performed to calibrate the system and compared in the end.

The first one was the photogrammetry method with the *AICON* software. Photogrammetry is the practice of determining the geometric properties of objects from photographic images [47]. This method allows the characterization of geometries with high accuracy but also comes with high preparation effort. All the steps of this method were taken carefully following the instructions of the CSP Video Tutorial Unit 4 on the DLR channel [47]. This approach represents a complex approach and requires material, time, and knowledge of the software used, resulting in very high precision in the determination of the parameters. Overall, the main effort was to collect images from several perspectives and angles of the structure shown in figure 4.9 that were afterward evaluated in the software AICON. In the structure, there are retroreflecting targets (coded and not coded) to highlight the point of interest and a reference system that is indispensable for precise and reliable measurement [46].

Figure 4.9: AICON system calibration method.

Photographed structure from different perspectives and angles. The metal structure contains, coded and not coded, retroreflecting targets and a reference system. The program AICON recognizes these points of interest and performs the calibration.

The second test was the Chessboard pattern method obtaining high-accuracy measurements of the shape and deformation. The Matlab code provided by Scaramuzza [48, 49, 50] was implemented in this project. Figure 4.10 shows images taken with the camera containing a known chessboard pattern and the different distances and perspectives, i.e extrinsic values. This procedure is fast, completely automatic, practical, and no prior knowledge is required [49]. The result of this work is a Matlab Toolbox, which requires minimum user interaction. Thus, it was only necessary to collect between 10 to 20 images of a known pattern, checkerboard, at different positions and orientations [48, 49, 50]. This method assumes that the imaging function can be described by a Taylor series expansion whose coefficients are estimated by solving a four-step least-squares linear minimization problem, followed by a non-linear refinement based on the maximum likelihood criterion [49]. After the calibration, the toolbox provides two functions (CAM2WORLD and WORLD2CAM) which express the relation between a given pixel point and it is the projection onto the unit sphere. This relation depends on the mirror shape and the intrinsic parameters of the camera [51].

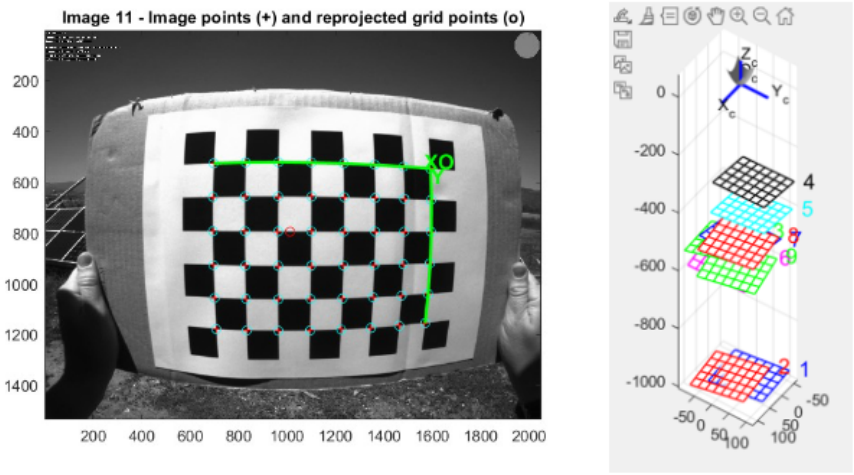

Figure 4.10: Chessboard pattern system calibration method.

During the calibration, between 10 and 20 images of a known chessboard pattern were required to take with the surveillance camera at different positions and orientations. The program recognizes the grid points and the extrinsic values.

In the end, both methods were compared and it was decided to use the AICON method. Despite similar results, the photogrammetry method has a greater accuracy, which was expected since it is a more complex process. However, it is highly recommended in the future to use the chessboard method due to it is advantages, for example, flexibility and time saving compared to the AICON method.

4.3.3 Generating Orthoimages

After processing all the images, figure 4.11 demonstrates all the steps to reach the main objective of this section: to generate orthoimages.

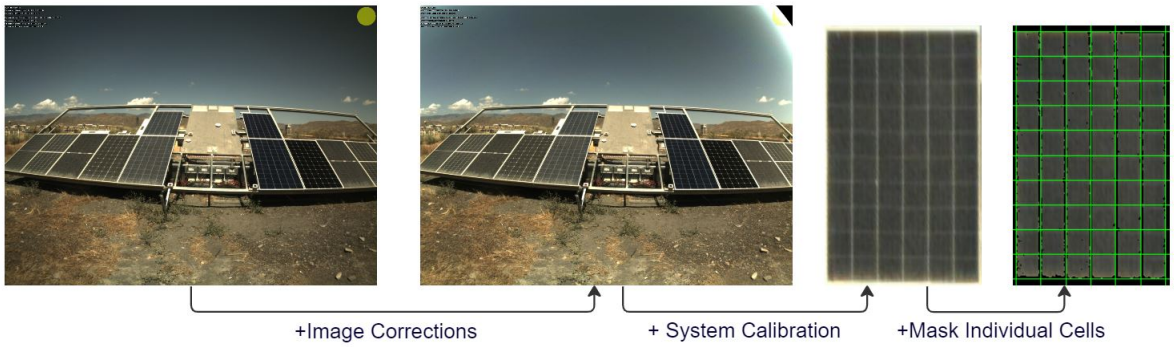

Figure 4.11: Data processing steps.

Captured image with all the settings from manufacturer turned off. Result after applying image corrections. System calibration to generate module orthoimages. Individual cell mask implemented.

The first image is one directly from the data acquisition. It is worth mentioning, that all the settings from the manufacturer were turned off and the exposure time is equal to 1280 microseconds, ensuring that the images can be compared. The next image is the result after applying imaging corrections. In this case, only the vignetting matrix since the gamma value for this exposure time is equal to one. The upper image's corners present wrong pixel values due to the drastic change in the vignetting matrix caused by the fitting problem between the camera and integrating sphere. Fortunately, as aforementioned, it is not relevant to the project, considering that the PV modules are located in the middle of the image and do not contain the strong brightness depicted. Later on, the system calibration is applied, which contains the interior and exterior orientation of the camera, which is required to create orthoimages of the PV Modules. Finally, a mask is created between spaces and conductor lines, to identify the cells.

4.4 Post Data Processing

After data processing, almost everything is ready to evaluate the soiling losses in the solar panels. First, the configuration parameters are processed, here it is defined the camera details. Afterward, all the images are analyzed and relevant information is retained, for example, angles and pixel value, which is organized on a Matlab structure. Then, image filtering takes place, to remove all the unusable images. Before the soiling evaluation, the program loads the clean and scattering calibration, done once and retained for future evaluations, which are an essential part of the equation referred to in chapter 4.1.2. Thus, in subsection 4.4.2 is explained the calibrations and how the variables were modeled. Finally, this section explains how the electrical reference output was calculated, which is fundamental in order to compare the generated results and to know the method's accuracy.

4.4.1 Data Information and Image Filtering

Before start the camera-based method, the program starts by reading the configuration file that was dedicated to this static camera case. Afterward, there is data treatment throughout all the raw images, processed images, and orthoimages, obtaining the information needed to calculate the soiling losses at the cell level. Therefore, for each image data, the time stamp and angles are known to describe: the sun position, camera position, solar panel position, and sun rays. Figure 4.12 demonstrates the PVsetup with the surveillance camera.

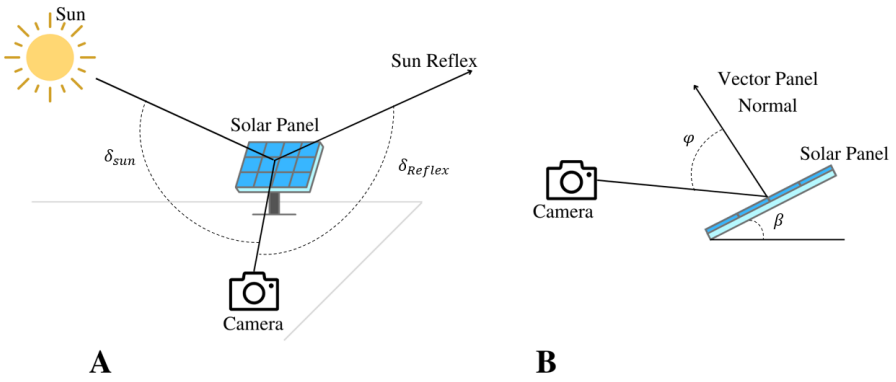

Figure 4.12: Configuration and data information, angle definition.
(A) δ_{sun} angle sun ray and camera; δ_{reflex} angle sun ray reflected and camera. (B) φ angle camera panel normal;β slope or tilt angle.

Besides the angles described in Chapter 3, four more angles were used in this project. Figure 4.12 A represents the camera vector, and direct and reflected sun ray. The angle between these two rays and the camera is the angle camera sun and angle camera sun reflex, respectively. On the right, figure 4.12 B, the different perspective allows to observe the angle between the vector panel normal and the camera vector, called the angle camera panel normal. Additionally, it is defined one more angle, angle azimuth camera normal, which is depicted in Figure 4.13.

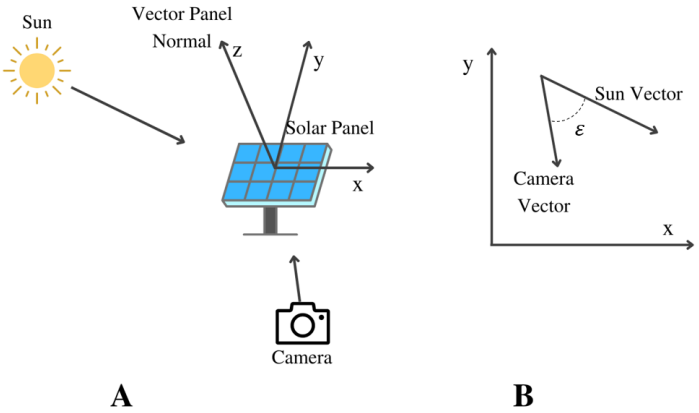

Figure 4.13: Configuration and data information, angle azimuth camera normal.
(A) Sun vector; camera vector; solar panel axis. (B) ϵ angle azimuth camera normal.

The part of figure 4.13 A, serves as an auxiliary drawing to understand figure 4.13 B. Camera vector and sun vector are projected in the plane of the solar panel, and the angle between the projections of these vectors is defined as the angle azimuth camera normal. One of the key aspects of knowing the different angles is due to the calibrations and evaluation, since the brightness of the soiling changes with the different sun and viewing positions.

Sun reflection on the images taken by the camera exhibit a general inhomogeneity in brightness. This particulary leads to the failure of the estimation of soiling losses since it looks brighter than it is in reality and overestimates the soiling losses. Figure 4.14 depicts modules 2 and 4 at a certain time on August 26^{th}. On one hand, figure 4.14 A presents sun reflexes. On the other hand, figure 4.14 B shows an image taken by the camera without sun reflexes.

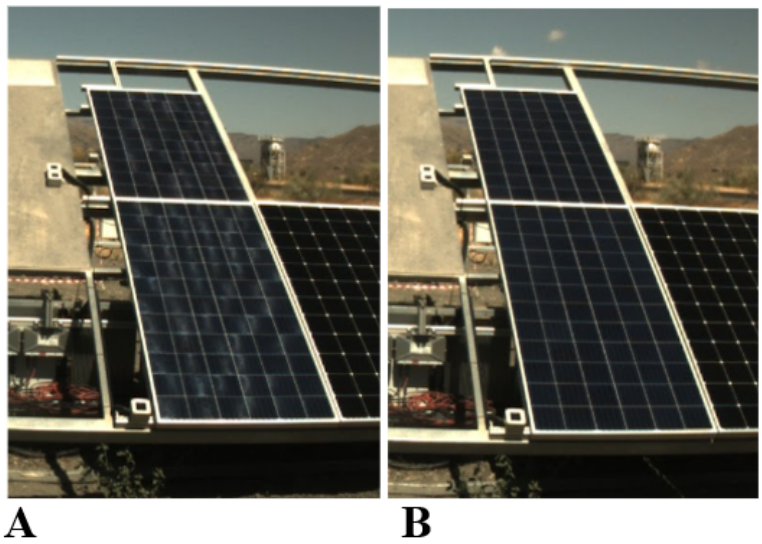

Figure 4.14: Module 2 and 4, August 26^{th}. Sun reflexes.
(A) - Sun reflex at 13:10:00; (B) - Without sun reflex at 14:00:00.

In that way, image filtering take place before the camera-based method starts to evaluate the images, where it is defined to analyze the image (1, logical value for true) or not analyze the image (0, logical value for false). Excluding from the evaluation the images that present sun reflexes.

4.4.2 Calibrations

Scattering calibration and clean calibration represent an indispensable steps in this project. The terms c_{scat} and E_{clean} from equation 4.1.2, are determined in the following subsections.

Scattering Calibration

Scattering parameters are dependent on the used camera and module technology. For that purpose, a plan was made to determine the scattering parameters with the static surveillance camera. As aforementioned, the brightness of a soiled module changes with the viewing and camera position. To model

this behavior, the camera recorded five different positions for six periods of time on the same day.

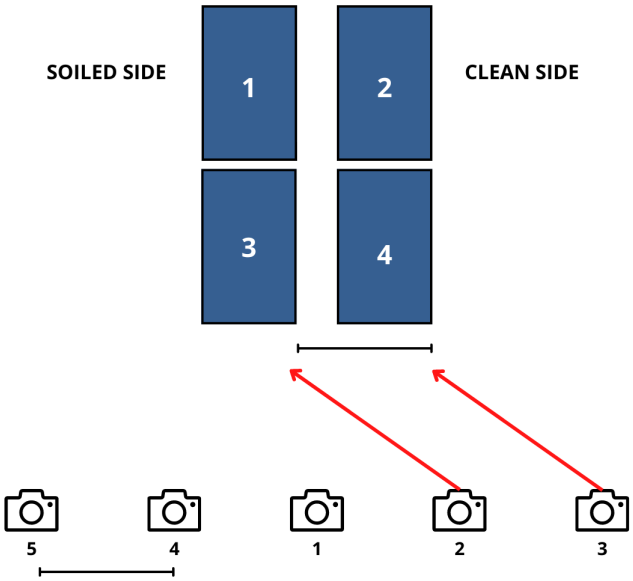

Figure 4.15: Positions in scattering calibration plan.

Five different camera positions to model the scattering behavior, with a known soiling ratio and clean reference. The positions are equidistant and are equal to the end-to-end of the PV module. Parallel lines ensure similar perspectives for the soiled and cleaned panels.

The different positions of the camera and the module's configuration are depicted in figure 4.15. For this calibration is necessary to know the energy losses due to soiling in modules 1 and 3 and to have a clean side reference, modules 2 and 4. The module comparison method is done, explained in more detail in subsection 4.4.3, to obtain the exact soiling losses of modules 1 and 3. Moreover, modules 2 and 4 were cleaned, to compare how the brightness changes between a known soiled module and a clean reference module. Thus, an important step in choosing the camera positions was the distance between positions, which is equal to the distance end-to-end of the solar panel 1 and 2 (or 3 to 4), as illustrated by the black line. This ensures that when the camera position is, for example, on position 2 and is evaluating the scattering behavior from the soiled modules (1 and 3), the similar viewing direction for the clean reference modules (2 and 4) corresponds to the camera position 3. To sum up, for each position the program evaluates, it will use the position on the right as a clean reference. In that way, camera position 3 is not used on the scattering behavior because there is not a clean reference for this position. This might be difficult to visualize, but one thing that can be helpful is drawing lines according to the viewing side; both lines need to be parallel. In this case, as illustrated, the scattering behavior of camera position 2 is being evaluated, and the clean reference used is from camera position 3 of the clean modules 2 and 4. The lines are alongside (parallel) and equidistant to the respective modules.

In Appendix A is possible to observe in more detail the experience to obtain the scattering parameters. The image frequency was 1 image per 15 seconds with a fixed exposure time of 1280 ms (mi-

croseconds). In total, over 1000 images were collected, without sun reflexes or other external factors, covering different sun positions during the day from five camera perspectives. The empirical function, c_{scat}, that defines the scattering light on the soiled module is described as dependent on 3 angles: angle camera sun reflex; angle camera panel normal, and angle azimuth camera normal.

Is desirable to have only one scattering calibration at the end of the experiment. However, this was not possible to achieve, since the different modules appeared to have a considerable disparity in energy losses. Although optically the two modules did not show a soiling ratio difference, the electrical output reference calculated revealed to have soiling losses around 2% and 3.5% for modules 1 and 3, respectively. One explanation could be the two bird drops located in module 3. Figure 4.16, is an image of module 3 from the calibration day, two bird drops can be spotted on the upper part of the PV panel. Bird drops cause a decrease in energy efficiency and could result in a miss match between the brightness observed and the actual energy losses due to soiling (explained in detail in the results section 5). Other motive, could be a problem in the scattering calibration itself for module 3 or an electrical output reference issue. Hence, two scattering calibrations were made individually and evaluated in the results chapter 5.

Figure 4.16: Module 3, two bird drops highlighted. September 5^{th}, calibration day.

Posterior to the calibration, the program displays the soiling losses plot. In this case, it can not be considered a result since the program knows the electrical reference output to perform the scattering calibration. Nevertheless, it is good to verify if it can calculate correctly the soiling losses at the module level, and the cell level if it makes sense the different soiling rates. Below are presented both calibrations in the figures 4.17, 4.18, with an appropriate label of the modules and the correspondingly soiling losses bar at the cell level with a color map from dark blue to dark red, dark red as the maximum (5% and 10%) and dark blue as the minimum (0%).

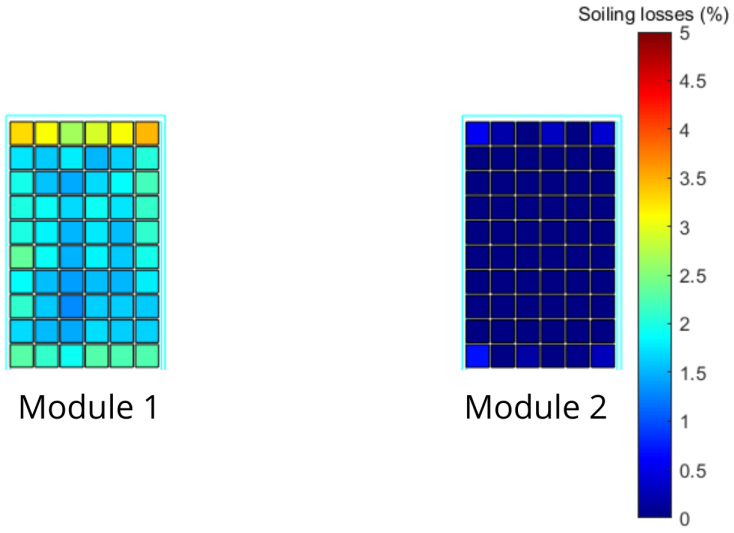

Figure 4.17: Soiling plot for modules 1 and 2. Scattering calibration.

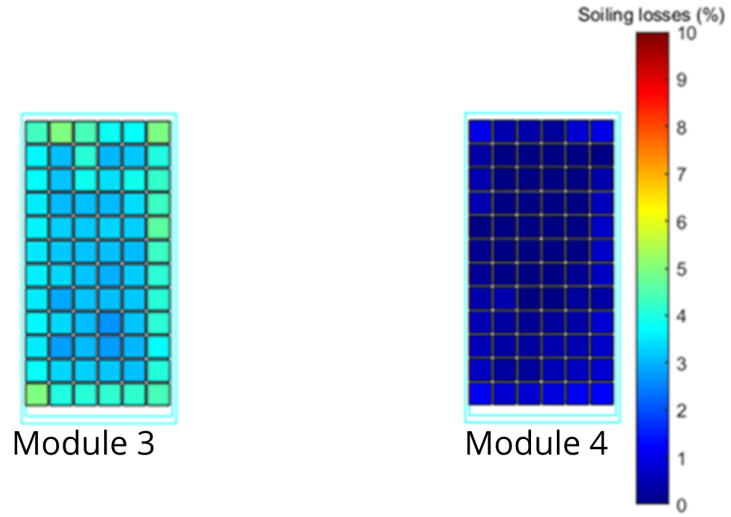

Figure 4.18: Soiling plot for modules 3 and 4. Scattering calibration.

In general, the soiling losses at the solar cell level are according to the brightness seen in the images. However, in module 1 the image has overexposed pixel values on the upper edge of the module due to the individual cell mask, which presents a systematic error. Further details and future recommendations are discussed later to overcome this issue. In addition, despite all the efforts to clean modules 2 and 4, some cells present minor soiling. This is normal since some of the particles are hard to remove, particularly on the corners and edges where it accumulates more dust, as the literature stresses.

The next table 4.2 presents the results of the individual calibrations and the respectively absolute and relative error in percentage, which is very small as expected since it is a calibration result. This proves that the calibration is done properly and can be used for forwarding evaluations.

Table 4.2: Camera-based method results for module 1 and 3. Scattering calibration.

	Module 1	**Module 3**
Electrical Output Reference (%)	1.84	3.60
Calculated Camera-Based Method (%)	1.85	3.65
Absolute Error	0.01	0.05
Relative Error (%)	5.43	1.38

Clean Calibration

Besides the scattering calibration, the soiling analysis program needs to load a clean calibration for all the modules. The previously discussed calibration plan, scattering calibration, was made precisely to avoid cleaning all the modules from the PV setup. In this way, in parallel with the scattering calibration, the same experiment served as clean calibration. The collected data was made in one clean calibration and like in the scattering calibration, and with Matlab, the brightness of the pixel value, E_{clean}, was defined as dependent on three angles: camera sun reflex, camera panel normal and angle azimuth camera normal.

4.4.3 Electrical Reference Measurement

Like any other scientific project, it is fundamental to have a reference to compare the results from the camera-based method developed. For that purpose, the module comparison method is used. One side of the PV setup is cleaned and the other side is naturally soiled. With the electrical output of the modules under study, the energy generated is compared and it is possible to know how much energy is wasted due to soiling. In this case, as mentioned before, module 1 is compared to module 2 and module 3 to module 4, due to the different cell types used. In addition, the daytime period used was equal to 1 hour and 15 minutes after and before the solar noon, which is the time when the sun appears to contact the local celestial meridian. In Tabernas desert in August, this time was around 2:15 pm. The sun and PV panels are facing south during this time and the results from this time interval are more reliable because there is no tilted angle influencing the results.

Although the compared modules are from the same manufacturer and technology, it is impossible to replicate the same module with the same energy efficiency. Hence, efficiency calibration was done on top of the module comparison method. For that matter, the modules were cleaned and for optimal conditions (clear sky day), the energy generated by the compared modules should be the same. The electrical output showed that module 1 was less efficient than module 2 and module 3 was more efficient than module 4, equations 4.7 and 4.8.

$$CF_{M1} = \frac{P_{Mc1}}{P_{Mc2}} = 0.99 \tag{4.7}$$

$$CF_{M3} = \frac{P_{Mc3}}{P_{Mc4}} = 1.03 \tag{4.8}$$

CF stands for the correction factor and M for the respective module under study. The P concerns the Power generated and c is to distinguish from a clean or soiled (s) module. Finally, equation 4.9 show how the final soiling ratio reference, SR, is obtained for modules 1 and 2 respectively, which contains the module comparison method divided by the correction factor calculated in the efficiency calibration. In addition, a simple mathematical calculation is done to have the soiling losses, SL, in percentage (%), equation 4.10.

$$SR_M = \frac{P_{Ms}}{P_{Mc}} / CF_M \tag{4.9}$$

$$SL_M(\%) = 1 - SR_M \tag{4.10}$$

Chapter 5

Results and Discussion

For every evaluation day performed, the clean side reference, modules 2 and 4, was cleaned and the electrical output reference was calculated. Without this step, it is not possible to ensure the liability on the electrical output reference with the module comparison method, described in chapter 4.4.3. In addition, the period of the images under study was equal to 2 hours and 15 minutes after and before the solar noon (local solar noon in August and September 2:15 pm). Furthermore, with the image filtering, none of the images with sun reflexes were evaluated. Moreover, the processed images and all the important information (e.g time stamp, angles, image Id, pixel value) are stored in a Matlab structure. Lastly, the clean and scattering calibrations are loaded, c_{scat} and E_{clean}.

$$E_{soiled} = E_{clean} \cdot \tau_{soiling}(\alpha_{sun}) \cdot \tau_{soiling}(\alpha_{camera}) + c_{scat}(\vec{r_{sun}}, \vec{r_{camera}}) \cdot E_{scat}(\tau_{soiling})$$

(5.1)

The total radiation from the soiled module is known from the image acquisition and the radiation being scattered depends on the quantity of soiling present in the module, $\tau_{soiling}$. There is only one unknown term in the equation 5, $\tau_{soiling}$, transmission optical losses also referred to as soiling losses of the modules. However, the results are presented separately due to the individual scattering calibrations. First, the results of modules 1 and 2 are presented, and later modules 3 and 4. To be able to make statistical statements, the absolute (E_{abs}) and relative errors ($E_{rel}\%$) are calculated (equations 5.2 and 5.3) and presented in a table format for each experiment.

$$E_{abs} = |SL_{Reference} - SL_{Camera}| \tag{5.2}$$

$$E_{rel}(\%) = \frac{E_{abs}}{SL_{Reference}} \cdot 100 \tag{5.3}$$

5.1 PV Modules 1 and 2

To validate the method and the modeled parameters, optimal meteorological conditions were pursued, that is, a clear sky day. Thus, ensuring there is no influence on the brightness due to clouds and the electrical data presents a smooth power curve over time. Only three days were found in optimal conditions to evaluate the method developed. Table 5.1 gives an overview of the results, pointing to the electrical output reference, the calculated camera-based method value and the respective absolute and relative errors. In this case, both errors, absolute and relative, are small, which indicates that the camera-based method can be validated successfully and used on days with optimal conditions with high accuracy, between 2% and 4%.

Table 5.1: Camera-based method results for module 1. Optimal meteorological conditions.

	Module 1		
	August 22^{nd}	August 26^{th}	September 15^{th}
Electrical Output Reference Soiling Losses (%)	6.4	6.7	1.1
Calculated Camera-Based Method Soiling Losses (%)	6.5	7.0	1.1
Absolute Error	0.1	0.3	0.0
Relative Error (%)	2.3	4.7	2.1

In the following figures 5.1, 5.2 and 5.3, it is possible to observe the final plot, called soiling plot, displayed at the end of the evaluation. For the three days under these circumstances, the respective soiling losses for each cell is presented, within the interval of 0 and 10 percent (%) and 0 and 5 percent (%). Although the method developed evaluates at the cell level, the electrical reference is only given at the module level. Nevertheless, important conclusions can be drawn to understand where more soiling is located and the reasons behind it.

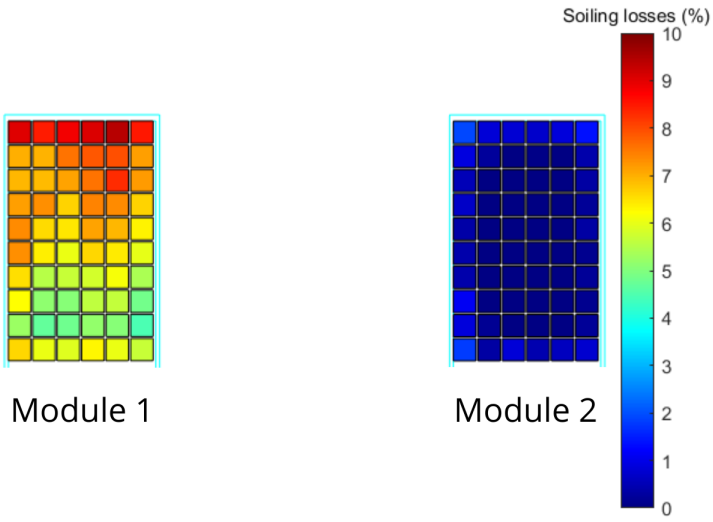

Figure 5.1: Soiling plot module 1 and 2, August 22^{nd}. Optimal meteorological conditions.

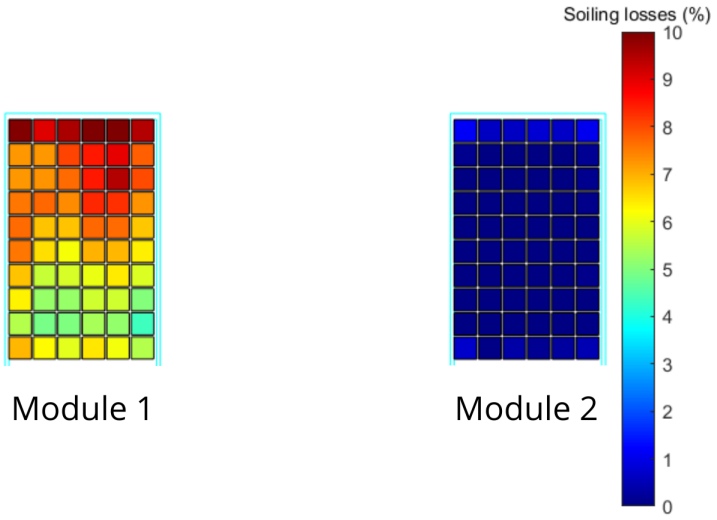

Figure 5.2: Soiling plot module 1 and 2, August 26^{th}. Optimal meteorological conditions.

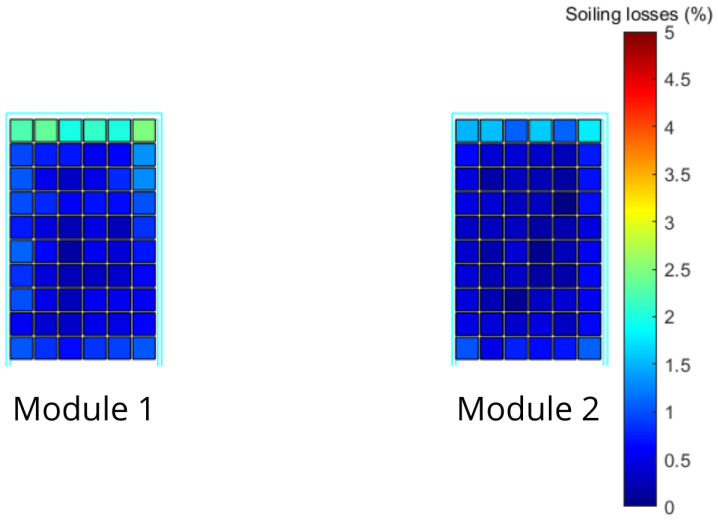

Figure 5.3: Soiling plot module 1 and 2, September 15^{th}. Optimal meteorological conditions.

Generally, the figures are consistent. Module 2, on the right, as expected, displays dark blue cells, around 0% or minimal soiling losses, since it is cleaned every day. However, lighter dark blue cells exist on the edges and corners, which translates into energy losses. Despite all the efforts to clean the modules, there is a small accumulation of dust on the edges, which is difficult or sometimes not possible to remove. In addition, the modules in question are difficult to reach, making it not an easy task to clean manually.

Regarding the soiled module on the left, module 1, there is stronger soiling in the upper part of the module. One thing that can explain this situation is the dust rain from the previous days. This phenomenon is common in the Western and Southern Mediterranean and happens when rain contains enough desert dust for the dust to be visible to the human eye [52]. Although rain dust also soils the modules, it also has a cleaning effect, since the water goes down with gravity and there is more cleaning effect on the lower part of the module. In addition, there is stronger soiling on the edges of the modules, normally dust particles are trapped in the metal edges of the PV panel, which goes along with the literature. Furthermore, for the very first row, 6 cells in the upper part, there might be overexposed pixel values due to the metal edges of the PV panel itself. Thus, might enhance the brightness depicted in the captured image and result in an evaluation error. Nevertheless, the method calculated the soiling losses successfully, and is visible a brightness increase is visible in the upper part of the PV soiled module, due to light scattered by dust particles.

After validating the camera base method, different meteorological conditions were tested, to observe how the results are influenced by diffuse irradiance. The meteorological conditions showed two days with a clear sky and some clouds. During the data acquisition, it is possible to observe shadows under different modules and at different times, but in general, the clear sky prevailed. The next table 5.2 presents the results under these circumstances.

Table 5.2: Camera-based method results for module 1. Clear sky with some clouds meteorological conditions.

	Module 1	
	August 25^{th}	September 8^{th}
Electrical Output Reference Soiling Losses (%)	6.3	2.5
Calculated Camera-Based Method Soiling Losses (%)	7.1	2.1
Absolute Error	0.8	0.4
Relative Error (%)	12.6	14.2

The results showed that despite the presence of some clouds, enhancing the diffuse irradiance, can estimate the soiling losses with 12% to 14% of accuracy. Like in the optimal conditions, the figures 5.4 and 5.5 are consistent and the cleaned modules present minimal losses in the corners and edges. In the soiled module, the upper part presents a higher soiling ratio, this might be for the same reasons explained before: dust rain and the individual cell mask.

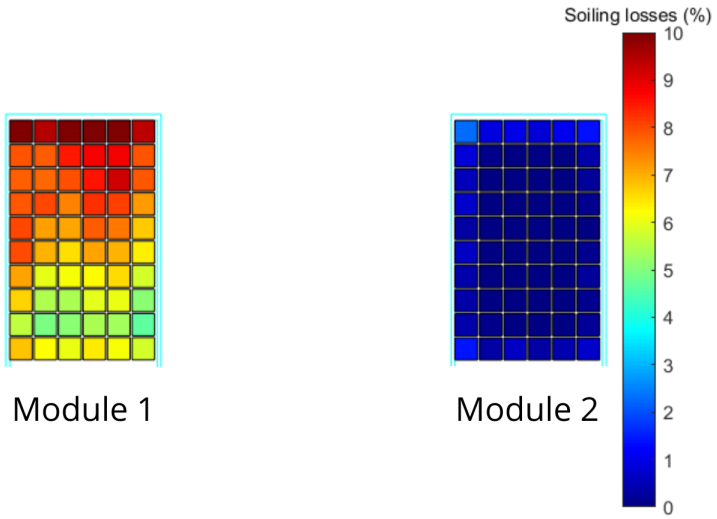

Figure 5.4: Soiling plot module 1 and 2, August 25^{th}. Clear sky with some clouds meteorological conditions.

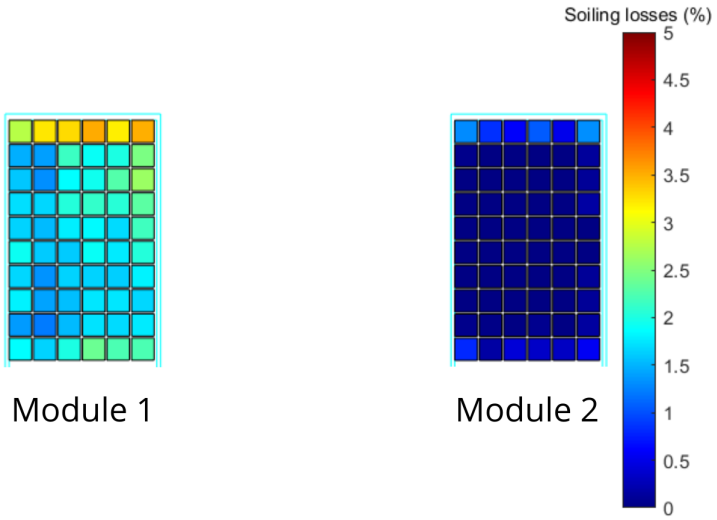

Figure 5.5: Soiling plot module 1 and 2, September 8^{th}. Clear sky with some clouds meteorological conditions.

The last evaluation performed was on a cloudy day. Here the method's failure under these conditions was witnessed. During the data acquisition, all the images looked dark and bright at the same time. Not only does the presence of clouds influence the shadows and darker images taken by the camera, but also increases the light scattered and diffuse irradiance. Table 5.2 presents the results obtained from the camera-based method. The outcome has a relative error of 672.1%.

Table 5.3: Camera-based method results for module 1. Cloudy meteorological conditions.

	Module 1
	September 2^{nd}
Electrical Output Reference Soiling Losses (%)	1.3
Calculated Camera-Based Method Soiling Losses (%)	9.7
Absolute Error	8.4
Relative Error (%)	672.1

At first sight, the soiling plot in figure 5.6, presents both modules (1 and 2) heavily soiled according to the camera-based method. Like in the previous evaluations, module 2 should appear dark blue with minimal losses in the corners, since it is cleaned every day. In addition, the soiling rate displayed in the two modules is high, around 6% and 10%. This is expected since the scattering light reaching the camera increases with the presence of adverse conditions, such as clouds, that contributes to the RGB pixel value. Nevertheless, a positive aspect of this evaluation is that, despite module 2 being soiled, the soiling rate compared to module 1 is lower. This is a good direction for future work.

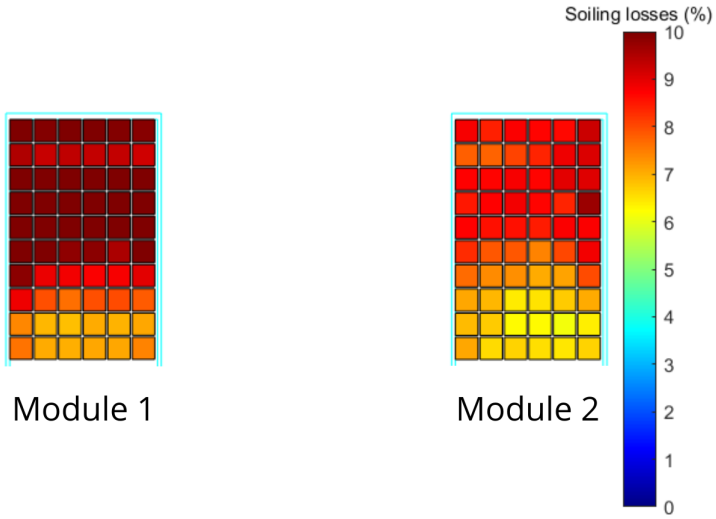

Figure 5.6: Soiling plot module 1 and 2, September 2^{nd}. Cloudy meteorological conditions.

5.2 PV Modules 3 and 4

For Modules 3 and 4, all the evaluations showed a relative error above 75%. For that reason, the method failed the validation process. Table 5.4, presents the results of the evaluations for optimal conditions, clear sky, which presented high accuracy in the upper modules (1 and 2).

Table 5.4: Camera-based method results for module 3. Clear sky meteorological conditions.

	Module 3	
	August 22^{nd}	August 26^{th}
Electrical Output Reference Soiling Losses (%)	8.8	10.3
Calculated Camera-Based Method Soiling Losses (%)	17.7	18.3
Absolute Error	8.8	8.1
Relative Error (%)	99.8	78.7

One possibility behind this situation is the bird drops located in the upper part of module 3. Despite being small, strongly affect the performance of solar PV cells [53]. In addition, the bird drop can cause a electrical miss matched effect, which can play a role on the energy efficiency decrease [54]. This method is not sensible to the electrical model of the PV module. Both soiled modules, 1 and 3, showed similar optical soiling on site. However, module 3 presented higher soiling of 3.5 percent (%) energy losses, a difference of 1,5 percent (%) compared to module 1. This value of 3.5 % relies on energy losses due to soiling and bird drops, but since the bird drops are small compared to the rest of the area of the PV module, the brightness of module 3 almost does not vary compared to the image of module 1. The input of $\tau_{soiling}$, during the scattering calibration will admit that for that specific brightness of the module the energy losses due to soiling are equal to 3.5%. If the empirical function (c_{scat}) to describe the scattering behavior, which is dependent on the camera and sun position, is estimated considering a certain energy loss that is not only caused by mainly dust soiling layer and has a significant impact on the energy losses, like the bird drops, this means that brightness of the module is overestimated in future evaluations.

Another possibility is an unknown problem that occurred during the scattering calibration itself or an issue in the electrical output reference. More efforts are needed to correct this mistake. However, due to time constraints and optimal weather condition dependence, it was not possible to study in depth. Nevertheless, the bird's drop is an interesting topic of study and the theory that is believed to be the origin of the problem in the scattering calibration.

Although the results showed a high inaccuracy when evaluating the soiled module (module 3), the clean module (module 4) displayed an expected value of 0%. This is proof that the inaccuracy of the results is coming from the scattering calibration.

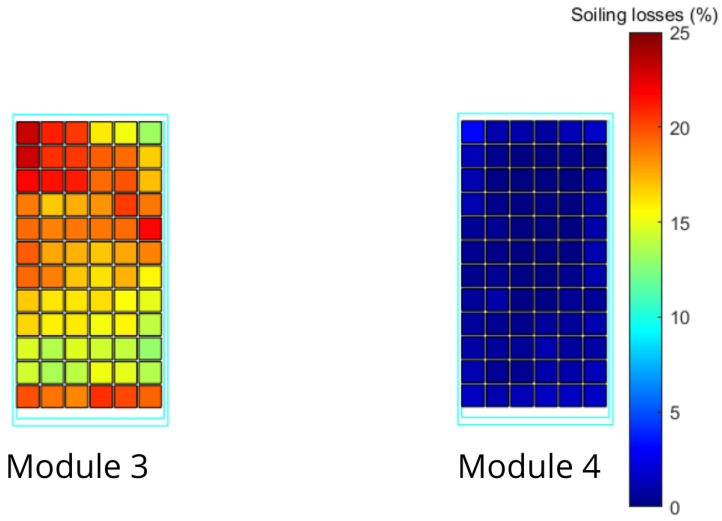

Figure 5.7: Soiling plot module 3 and 4, August 22^{nd}. Optimal meteorological conditions.

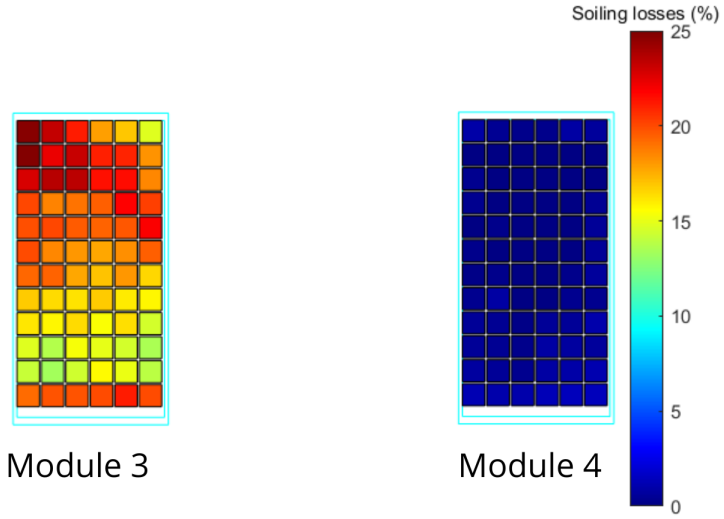

Figure 5.8: Soiling plot module 3 and 4, August 26^{th}. Optimal meteorological conditions.

Figures 5.8, 5.7 and table 5.4, confirm that for each case, the soiling losses are greater than the reference value. No further evaluations with different meteorological conditions are presented because the method did not pass successfully the validation process for modules 3 and 4.

However, perhaps, if the birds' drops did not exist on the calibration day, meaning that, both modules (1 and 3) would have a similar soiling loss, only one scattering calibration would have been performed. With that being said, if the future evaluation presented a certain brightness and contained bird drops, which not affecting significantly the brightness of the module, an offset could be added to the following equation 5 and calculate the soiling losses with the following equation 5.4.

$$\tau_{SoilingCorrected} = (1 - f_{BirdDrops}) \cdot \tau_{soiling} + f_{BirdDrops} \cdot \tau_{BirdDrop} \tag{5.4}$$

$\tau_{SoilingCorrected}$ represents the new soiling losses corrected value calculated with the presence of bird drops in the PV panel. Thus, the sum between the $\tau_{soiling}$ calculated with the camera-based method for the area, which do not contain the bird drops $(1 - f_{BirdDrops})$, and the factor $f_{BirdDrops}$, that is, the fraction between the area occupied by the birds drop divided by the total area of the panel, times the transmission losses of bird drop $\tau_{BirdDrop}$. Due to time constrains this theory was not possible to be tested, but future work is suggested to overcome this situation.

5.3 Method Limitations

In this section, the limitations verified in the camera-based method with the surveillance camera are mentioned. In this work, the scattering due to diffuse light is not taken into account, meaning adverse meteorological conditions are a limitation. The shadow variability due to clouds depicted in the captured images and the light scattered influence the outcome of the method. In subsection 5.1, an evaluation of a very cloudy day was made to witness the method's failure. Also, geometries with sun reflexes are avoided due to the overexposed pixel values on the digital image. In that way, image filtering is performed to exclude the unusable image, subsection *Image Filtering* **??**. Moreover, the pixel brightness scales with global illumination in the tilted plane. In addition, although the method calculates the soiling losses at the cell level, the electrical output reference is from the module itself. Thus, the mean value of the soiling losses over all cells is performed and this corresponds to the soiling losses of the module. Furthermore, bird drops were found to be another limitation of this method, especially if the scattering and clean calibrations are performed under these circumstances. Although do not affect substantially the brightness of the soiled module, it has an impact on the energy losses. In that way, when calculating the soiling losses with the camera-based method this represents a false perception of the brightness for the rate of soiling losses verified. Lastly, the electrical miss match effect is not taken into consideration in this method. If there is a strong inhomogeneity on the deposited soiling in the PV module or a cell that is strongly soiled, the electrical model needs to be taken into consideration. IV-characteristics are a viable way to reproduce electrical network behavior [54]. Therefore it is important to check if the IV curve presents a similar curve shape between the cleaned state and the soiled state. To test this, two experiments were performed. The first graphic presented in figure 5.9 presents the IV curves for two modules, in which module 2 is completely cleaned and module 1 is naturally soiled.

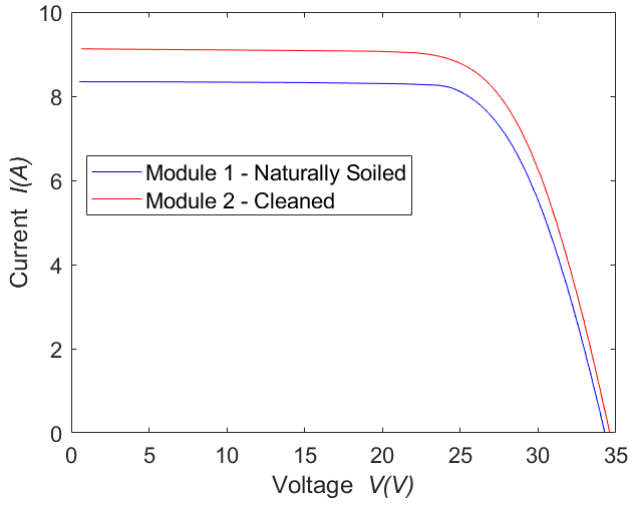

Figure 5.9: IV curve for August 26^{th}, 3pm UTC+1, for module 1 and 2.

In the second graphic, figure 5.10, module 2 is cleaned as in the first case, but one substring of module 1 was cleaned, figure 5.11. Thus, resulting in an electrical miss match.

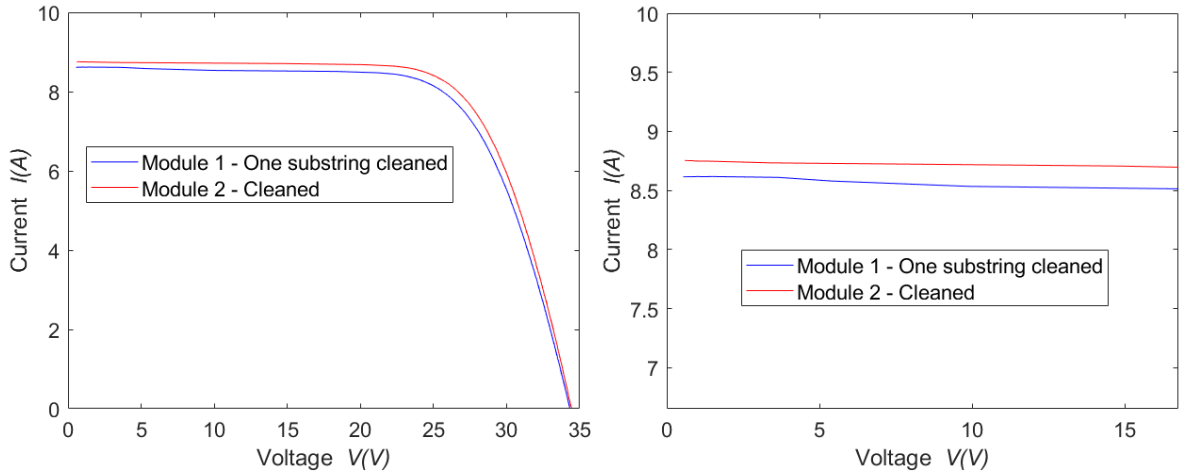

Figure 5.10: IV curve for September 10^{th}, 3pm UTC+1, for module 1 and 2.

Figure 5.11: Module 1, one substring cleaned. Electrical miss match experience, September 8^{th}.

The start of the IV curve in figure 5.10 for module 1, presents an irregular IV curve shape, which is highlighted on the right of the figure. The zoom-in makes clear the different trajectories of the curves. This is due to the electrical miss match effect caused by the one-third cleaned module. If a series of cells contains different mismatched IV curves, the operating current at the maximum power point of the overall system is not coinciding with the maximum power point of each cell [54]. In comparison with figure 5.9 depicts a similar curve shape for the two modules. For that matter, it is important to verify the electrical miss effect presence before using the method. The IV curves are a practical and fast way to check as demonstrated.

Chapter 6

Conclusions

In this chapter, the main conclusions of this report are stated, followed by future recommendations. Initially, data acquisition and the respective settings were discussed. Next, the image corrections and system calibrations took place, to correct all the digital image effects and distortion of the captured wide-angle surveillance camera. In that way, by combining these four steps, it was possible to create correct orthoimages and later with the applied mask, individual cell orthoimages. In addition, scattering and clean calibration were done by side. Afterward, with these two inputs, image data, and the calibrations, the developed method runs the program, and with image filtering, excludes all the unusable images. Reaching the ultimate goal, that is, to calculate the energy losses in the PV panels due to soiling. Finally, the results were compared with the electrical output reference, which was corrected by an efficiency calibration.

First of all, it is important to interpret the results of the validation meaningfully. The validation of the method was successful for modules 1 and 2, obtaining for optimal conditions an accuracy to determine soiling losses between 2% and 4%. The results with different meteorological conditions provided deeper insights into how the variability of the clouds influences the outcome. For the moment, it can be stated that, for clear sky conditions or clear sky with some clouds, the method can predict with good accuracy. However, it is worth mentioning that only local soiling/dust from PSA (Plataforma Solar de Almería) was evaluated. If the soiling conditions change, it's necessary to perform a new scattering and clean calibration, because the evaluation is dependent on dust properties. Regarding a very cloudy day, the method accuracy decreases significantly to 672%.

The results from modules 3 and 4 revealed undesirable output and failed the validation process. After a detailed analysis of the module in question, both modules 1 and 3 on-site presented optically the same soiling, which means that both modules should have a similar soiling ratio. The only difference between modules was, module 3 had two bird drops. One possibility behind the wrong calibration is the bird drops located in the upper part of module 3. Despite being small, strongly affect the performance of solar PV cells [53]. Another possibility is an unknown problem that occurred during the scattering calibration or an electrical output reference issue. Nevertheless, the bird's drop is an interesting topic of study and the theory that is believed to be the origin of the problem caused in the scattering calibration.

One more limitation needs to be added to the method and future work needs to address this matter. However, for the same evaluation, the clean reference module showed to be accurate and showed 0% of soiling losses. This indicates that the scattering calibration of module 3 is the only wrong input in the method, which overestimates the soiling losses and it is believed that is due to bird drops that significantly influence the energy efficiency outcome, but do not affect the brightness that the camera captures.

A key recommendation is to perform the soiling analysis during the solar noon because there is no title angle influencing the results and the image is clearer. The sun, panels, and camera are facing south and a line can be drawn from the sun until the panels pass through the camera, making it more likely to have direct scattering into the camera. Thus, having sun reflections on the images produces a brightness inhomogeneity in the PV modules. In that way, another proposal is to fix the camera not directly in the center, but on the side, avoiding sun reflexes on the collected data during the solar noon.

Overall, this new camera-based method provides live data, which can be accessed and treated easily. Additionally, it can be used in large areas, for example, in a PV park, in contrast to the soiling measurements commercially available [13]. Furthermore, if the PV park already has installed surveillance cameras on site for security or monitoring purposes, it can also be used to evaluate the energy losses due to soiling without needing extra efforts and new installations. Not only it is used normally for security reasons, but also can be used to optimize the energy efficiency of all parks. In this case, with the soiling analysis evaluations and with a large amount of data, it is possible to optimize the cleaning schedule.

6.1 Outlook

Finally, it is shown what this work laid the foundation for and what future questions and tasks could be. Although the growing interest in soiling mitigation in solar technology due to the impact on the maintenance and economics of solar energy plants, when compared to the amount of research in other fields in the solar power industry and research community, such as PV cell development, some research is lacking to address this problem [11].

This project demonstrates a valid solution for the detection of soiling in the PV solar energy, and how it can affect the energy efficiency of the process. However, further developments are needed. For one, a larger data set will improve the validation of the extended formula and a sensitivity study will reveal which part of the formula has the greatest potential for improvement. To evaluate a larger data set, it is necessary to have more surveillance cameras installed in the solar plant and/or with a larger overseeing area. Furthermore, recent/modern surveillance cameras are recommended due to their pixel resolution. Due to time constraints, it was only possible to test the model with a fixed exposure time. In this sense, future research should consider dynamic exposure time. Another sensitivity research proposal would be to test this approach for different types of PV modules and various types of soiling. The last recommendation would be to consider shading by bird drops, explained in the subsection 5.2.

Following these recommendations represents a novel set of derived project opportunities for production in the solar energy industry. The increased predictability of production is followed by further research questions, such as how soiling detection methods can help in the soiling mitigation techniques (cleaning method), or how fast can be the evaluation of whole PV parks.

Bibliography

[1] Climate actions. the science: What is climate change? *United Nations*, https://www.un.org/en/climatechange/what-is-climate-change, Accessed: 22-04-2022.

[2] Renewable energy is key to fighting climate change. *NRDC*, 2016. https://www.nrdc.org/experts/noah-long/renewable-energy-key-fighting-climate-change, Accessed: 23-04-2022.

[3] Soteris A. Kalogirou, Rafaela Agathokleous, and Gregoris Panayiotou. On-site pv characterization and the effect of soiling on their performance. *Energy*, 51:439–446, 2013.

[4] Future of solar photovoltaic: Deployment, investment, technology, grid integration and socio-economic aspects (a global energy transformation: paper). *IRENA, International Renewable Energy Agency*, Abu Dhabi 2019. https://www.irena.org/publications/2019/Nov/Future-of-Solar-Photovoltaic.

[5] Hai Jiang, Lin Lu, and Ke Sun. Experimental investigation of the impact of airborne dust deposition on the performance of solar photovoltaic (pv) modules. *Atmospheric Environment*, 45(25):4299–4304, 2011.

[6] International Energy Agency. *World Energy Outlook 2021, IEA, . Licence: Creative Commons Attribution CC BY-NC-SA 3.0 IGO*. 2021. https://www.iea.org/reports/world-energy-outlook-2021.

[7] Eia. *Solar explained, Photovoltaics and electricity*. https://www.eia.gov/energyexplained/solar/photovoltaics-and-electricity.php, Accessed: 23-04-2022.

[8] Steven S. Hegedus and Antonio Luque. *Status, Trends, Challenges and the Bright Future of Solar Electricity from Photovoltaics*, chapter 1, pages 1–43. John Wiley Sons, Ltd, 2003.

[9] Sayak Bhattacharya and Sajeev John. Beyond 30% conversion efficiency in silicon solar cells: A numerical demonstration. *Scientific Reports*, 9, 08 2019.

[10] Klemens Ilse, Leonardo Micheli, Benjamin W. Figgis, Katja Lange, David Daßler, Hamed Hanifi, Fabian Wolfertstetter, Volker Naumann, Christian Hagendorf, Ralph Gottschalg, and Jörg Bagdahn. Techno-economic assessment of soiling losses and mitigation strategies for solar power generation. *Joule*, 3(10):2303–2321, 2019.

[11] Monto Mani and Rohit Pillai. Impact of dust on solar photovoltaic (pv) performance: Research status, challenges and recommendations. *Renewable and Sustainable Energy Reviews*, 14(9):3124–3131, 2010.

[12] Felix Terhag, Fabian Wolfertstetter, Stefan Wilbert, Tobias Hirsch, and Oliver Schaudt. Optimization of cleaning strategies based on ann algorithms assessing the benefit of soiling rate forecasts. volume 2126, page 220005, 07 2019.

[13] Michael Gostein, Stan Faullin, Keith Miller, Jason Schneider, and Bill Stueve. Mars soiling sensor™. *2018 IEEE 7th World Conference on Photovoltaic Energy Conversion (WCPEC) (A Joint Conference of 45th IEEE PVSC, 28th PVSEC & 34th EU PVSEC)*, pages 3417–3420, 2018.

[14] DLR. Pv symposium 2023. d5 spatially resolved determination of contamination of pv modules with surveillance cameras. dlr, almeria, spain. : https://www.pv-symposium.de/.

[15] Suellen C.S. Costa, Antonia Sonia A.C. Diniz, and Lawrence L. Kazmerski. Dust and soiling issues and impacts relating to solar energy systems: Literature review update for 2012–2015. *Renewable and Sustainable Energy Reviews*, 63:33–61, 2016.

[16] Travis Sarver, Ali Al-Qaraghuli, and Lawrence L. Kazmerski. A comprehensive review of the impact of dust on the use of solar energy: History, investigations, results, literature, and mitigation approaches. *Renewable and Sustainable Energy Reviews*, 22:698–733, 2013.

[17] Lawrence Kazmerski, Mohammed Jardan, Yasser Jnoobi, Yousef Shaya, and Jim John. Ashes to ashes, dust to dust: Averting a potential showstopper for solar photovoltaics. pages 0187–0192, 06 2014.

[18] Michael Gostein, Tim Düster, and Christopher Thuman. Accurately measuring pv soiling losses with soiling station employing module power measurements. In *2015 IEEE 42nd Photovoltaic Specialist Conference (PVSC)*, pages 1–4, 2015.

[19] Fardila Mohd Zaihidee, Saad Mekhilef, Mehdi Seyedmahmoudian, and Ben Horan. Dust as an unalterable deteriorative factor affecting pv panel's efficiency: Why and how. *Renewable and Sustainable Energy Reviews*, 65:1267–1278, 2016.

[20] Reinhart Appels, Buvaneshwari Lefevre, Bert Herteleer, Hans Goverde, Alexander Beerten, Robin Paesen, Klaas De Medts, Johan Driesen, and Jef Poortmans. Effect of soiling on photovoltaic modules. *Solar Energy*, 96:283–291, 2013.

[21] Dirk Goossens. Soiling of photovoltaic modules: Size characterization of the accumulated dust. *Journal of Clean Energy Technologies*, 7:25–31, 05 2019.

[22] Hamdy Elminir, Ahmed Ghitas, Rabab Hamid, Fathy El-Hussainy, M.M. Beheary, and Khaled Abdel-Moneim. Effect of dust on the transparent cover of solar collectors. *Energy Conversion and Management*, 47:3192–3203, 11 2006.

[23] Juergen Sutterlueti, S Ransome, R Kravets, and Ludwig Schreier. Characterising pv modules under outdoor conditions: What's most important for energy yield. 01 2011.

[24] A. Massi Pavan, A. Mellit, and D. De Pieri. The effect of soiling on energy production for large-scale photovoltaic plants. *Solar Energy*, 85(5):1128–1136, 2011.

[25] Rob W. Andrews and Joshua M. Pearce. Prediction of energy effects on photovoltaic systems due to snowfall events. In *2012 38th IEEE Photovoltaic Specialists Conference*, pages 003386–003391, 2012.

[26] M. Korevaar, J. Mes, and X. van Mechelen. Measuring the sun the components of solar radiation, traceability of measurements, and pv panel soiling. In *Light, Energy and the Environment*, page RTh2B.1. Optica Publishing Group, 2017.

[27] Lawrence Dunn, Bodo Littmann, J. Riley Caron, and Michael Gostein. Pv module soiling measurement uncertainty analysis. In *2013 IEEE 39th Photovoltaic Specialists Conference (PVSC)*, pages 0658–0663, 2013.

[28] Benjamin W. Figgis, Ahmed Ennaoui, Saïd Ahzi, and Yves Rémond. Review of pv soiling measurement methods. *2016 International Renewable and Sustainable Energy Conference (IRSEC)*, pages 176–180, 2016.

[29] Wai Kean Yap, R. P. GALEt, and K. C. Yeo. Quantitative analysis of dust and soiling on solar pv panels in the tropics utilizing image-processing methods. 2015.

[30] Muhammed Unluturk, Ahmet Afşin Kulaksız, and Ali Unluturk. Image processing-based assessment of dust accumulation on photovoltaic modules. *2019 1st Global Power, Energy and Communication Conference (GPECOM)*, pages 308–311, 2019.

[31] Christoph Prahl, Badrudin Stanicki, Christoph Hilgert, Steffen Ulmer, and Marc Röger. Airborne shape measurement of parabolic trough collector fields. *Solar Energy*, 91:68–78, 2013.

[32] Christoph Prahl, Laura Porcel, Marc Röger, and Niels Algner. Airborne characterization of the andasol 3 solar field. volume 2033, 09 2017.

[33] John A. Duffie and William A. Beckman. Wiley. Solar engineering of thermal processes. *Solar Energy*, 28(1):85, 1982.

[34] Kakoli Saha. Planning and installing photovoltaic system: a guide for installers, architects and engineers. *International Journal of Environmental Studies*, 71, 11 2014.

[35] Rafael C. Gonzalez. *Digital image processing / Rafael C. Gonzalez, Richard E. Woods.* Prentice Hall, Upper Saddle River, N.J, 2nd ed. edition, 2002.

[36] Mohsen Manutchehr-Danai. *Young-Helmholtz theory of color vision*, pages 935–935. Springer Berlin Heidelberg. ISBN: 978-3-540-72816-0., 2009.

[37] Richard Perez, James Schlemmer, Karl Hemker, Sergey Kivalov, Adam Kankiewicz, and Christian Gueymard. Satellite-to-irradiance modeling - a new version of the suny model. In *2015 IEEE 42nd Photovoltaic Specialist Conference (PVSC)*, pages 1–7, 2015.

[38] P. Kuhn, S. Wilbert, C. Prahl, D. Schüler, T. Haase, T. Hirsch, M. Wittmann, L. Ramirez, L. Zarzalejo, A. Meyer, L. Vuilleumier, P. Blanc, and R. Pitz-Paal. Shadow camera system for the generation of solar irradiance maps. *Solar Energy*, 157:157–170, 2017.

[39] C Gueymard and F Vignola. Determination of atmospheric turbidity from the diffuse-beam broadband irradiance ratio. *Solar Energy*, 63(3):135–146, 1998.

[40] Mobotix. *Lens table*. `https://www.mobotix.com/sites/default/files/2021-01/Mx_LensTable_Mx6_en_210104.pdf`, Accessed: 03-05-2022.

[41] Wikipedia contributors. Demosaicing — Wikipedia, the free encyclopedia. `https://en.wikipedia.org/w/index.php?title=Demosaicing&oldid=1113926952`, 2022. [Online; accessed 27-October-2022].

[42] Richard Szeliski. *Computer Vision - Algorithms and Applications.* Texts in Computer Science. Springer. ISBN: 978-1-84882-935-0, 2011.

[43] Pranali Dhane, Krishnan Kutty, and Sachin Bangadkar. A generic non-linear method for fisheye correction. *International Journal of Computer Applications*, 51:58–65, 08 2012.

[44] Michael D. Grossberg and Shree K. Nayar. What can be known about the radiometric response from images? In Anders Heyden, Gunnar Sparr, Mads Nielsen, and Peter Johansen, editors, *Computer Vision — ECCV 2002*, pages 189–205, Berlin, Heidelberg, 2002. Springer Berlin Heidelberg.

[45] A. Rosebrock. *Deep Learning for Computer Vision with Python: Starter Bundle.* PyImageSearch, PyImageSearch. https://books.google.pt/books?id=9Ul-tgEACAAJ 2017.

[46] Robert Godding. 6 - geometric calibration of digital imaging systems. In Bernd Jähne and Horst Haußecker, editors, *Computer Vision and Applications*, pages 153–175. Academic Press, San Diego, 2000.

[47] Christoph Prahl DLR. Csp video tutorial unit 4, photogrammetry. : https//www.youtube.com/channel/UCvmIn3AxofQ5zXYKIYzAcYg/videos.

[48] Davide Scaramuzza, Agostino Martinelli, and Roland Y. Siegwart. A flexible technique for accurate omnidirectional camera calibration and structure from motion. *Fourth IEEE International Conference on Computer Vision Systems (ICVS'06)*, pages 45–45, 2006.

[49] Davide Scaramuzza, Agostino Martinelli, and Roland Siegwart. A toolbox for easily calibrating omnidirectional cameras. In *2006 IEEE/RSJ International Conference on Intelligent Robots and Systems*, pages 5695–5701, 2006.

[50] D Scaramuzza. Omnidirectional vision: from calibration to robot motion estimation, eth zurich, phd thesis no. 17635. phd thesis advisor: Prof. roland siegwart. committee members: Prof. patrick rives (inria sophia antipolis), prof. luc van gool (eth zurich). chair: Prof. lino guzzella (eth zurich), zurich. *ETH Zurich*, 2008.

[51] Martin Rufli, Davide Scaramuzza, and Roland Siegwart. Automatic detection of checkerboards on blurred and distorted images. In *2008 IEEE/RSJ International Conference on Intelligent Robots and Systems*, pages 3121–3126, 2008.

[52] Wikipedia contributors. Rain dust — Wikipedia, the free encyclopedia. `https://en.wikipedia.org/w/index.php?title=Rain_dust&oldid=1116153124`, 2022. [Online; accessed 22-October-2022].

[53] Anil Sisodia and Ram Kumar Mathur. Impact of bird dropping deposition on solar photovoltaic module performance: a systematic study in western rajasthan. *Environmental Science and Pollution Research*, 26, 10 2019.

[54] M. Alonso-Garcia and J.M. Ruíz. Analysis and modelling the reverse characteristic of photovoltaic cells. *Solar Energy Materials and Solar Cells*, 90:1105–1120, 05 2006.

Appendix A

Scattering Calibration

Table A.1: Time Schedule Scattering calibration. Positions and Rounds.

Position \Round	Round 1	Round 2	Round 3	Round 4	Round 5
Position 1	08:24/08:50	10:05/11:06	12:12/12:50	13:43/13:57	15:11/15:30
Position 2	08:53/09:09	11:09/11:23	12:52/13:03	13:59/14:11	15:31/15:48
Position 3	09:11/09:26	11:25/11:38	13:05/13:18	14:12/14:29	15:50/16:08
Position 4	09:29/09:38	11:41/11:57	13:20/13:29	14:31/14:41	16:11/16:28
Position 5	09:43/10:01	11:59/12:10	13:31/13:40	14:43/15:09	16:31/16:45

Table A.2: Clean Reference Position to Scattering Calibration.

	Clean Reference
Position 1	Position 2
Position 2	Position 3
Position 3	-
Position 4	Position 1
Position 5	Position 4

Figure A.1: Calibration day, September 5^{th}. Position 1.

Figure A.2: Calibration day, September 5^{th}. Position 2.

Figure A.3: Calibration day, September 5^{th}. Position 3.

Figure A.4: Calibration day, September 5^{th}. Position 4.

Figure A.5: Calibration day, September 5^{th}. Position 5.

Appendix B

Data Acquisition

Figure B.1: Optimal Conditions, clear sky. August 26th, 2:15pm UTC+1.

Figure B.2: Clear Sky with some clouds. August 25th, 2:15pm UTC+1.

Figure B.3: Cloudy day. September 2nd, 2:15pm UTC+1.

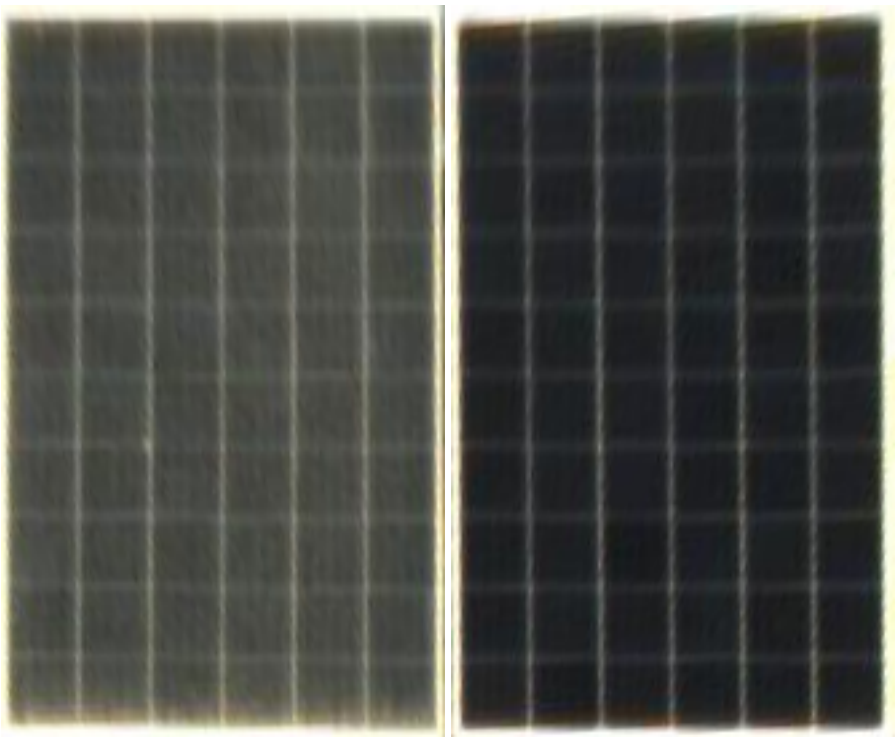

Figure B.4: Module orthoimage. Right side, module 1, Left side, module 2. August 26th, 2:15pm UTC+1.

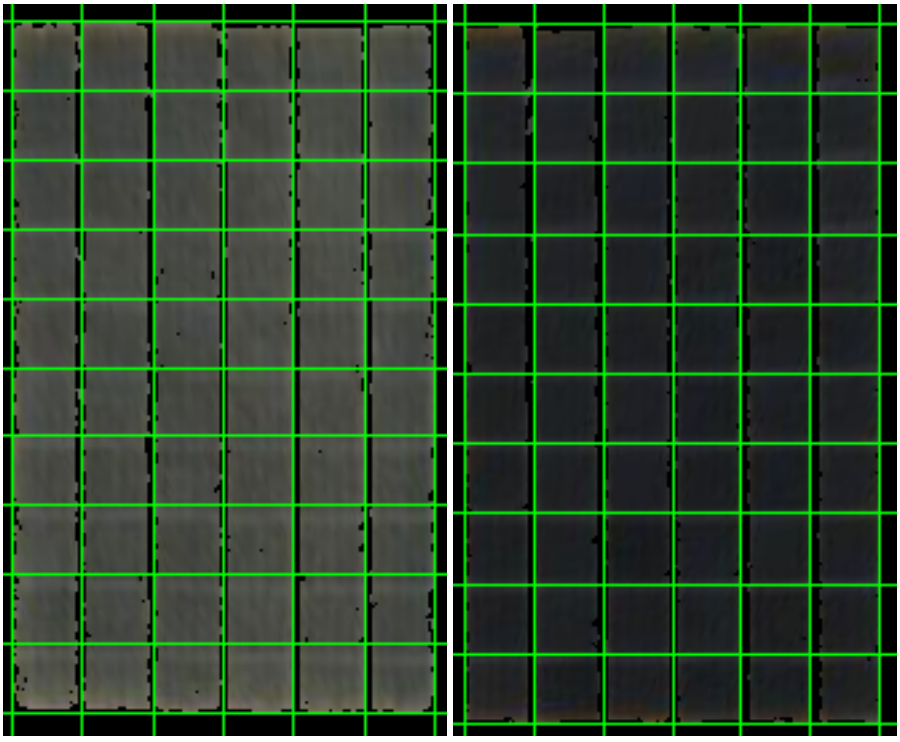

Figure B.5: Individual cell mask. Right side, module 1, Left side, module 2. August 26th, 2:15pm UTC+1.